Evidence for Low-pressure Crustal Anatexis During the Northeast Atlantic Break-up

A.M. Morris[1], S. Lambart[1], M.A. Stearns[2], J.R. Bowman[1], M.T. Jones[3], G.T.F. Mohn[4], G. Andrews[5], J. Millet[6,7], C. Tegner[8], S. Chatterjee[9], J. Frieling[10], P. Guo[11], C. Berndt[12], S. Planke[3,7,] C.A., Alvarez Zarikian[13], P. Betlem[3,14], H. Brinkhuis[15], M. Christopoulou[16], E. Ferre[17], I.Y. Filina[18], D. Harper[1], D.W. Jolley[6], J. Longman[19], R.P. Scherer[16], N. Varela[20], W. Xu[21], S.L. Yager[22], A. Agarwal[23], V.J. Clementi[24]

[1]Geology & Geophysics Department, University of Utah, Salt Lake City, UT, USA

[2]Department of Earth Sciences, Utah Valley University, Orem, UT, USA

[3]Department of Geosciences, University of Oslo, Oslo, Norway

[4]Laboratoire Géosciences et Environnement Cergy, University of Cergy-Pontoise, Cergy, France

[5]School of Environmental Sciences, University of Hull, Hull, UK

[6]Department of Geology and Geophysics, University of Aberdeen, King's College, Aberdeen, UK

[7]Volcanic Basin Energy Research AS, Høienhold, Oslo, Norway

[8]Department of Geoscience, Aarhus University, Aarhus, Denmark

[9]Earthquake Research Institute, The University of Tokyo, Bunkyō, Tokyo, Japan

[10]Department of Earth Sciences, The University of Oxford, Oxford, UK

[11]Institute of Oceanology, Chinese Academy of Sciences, Qingdao, China

[12]GEOMAR Helmholtz Centre for Ocean Research Kiel, Kiel, Germany

[13]International Ocean Discovery Program, Texas A&M University, College Station, TX, USA

[14]Department of Artic Geology, The University Centre in Svalbard, Svalbard, Norway

[15]NIOZ Royal Netherlands Institute for Sea Research, Den Burg, Texel, Netherlands

[16]Department of Earth, Atmosphere and Environment, Northern Illinois University, DeKalb, IL, USA

[17]School of Geoscience, University of Louisiana at Lafayette, Lafayette, LA, USA

[18]Department of Earth and Atmospheric Sciences, University of Nebraska, Lincoln, NE, USA

[19]Department of Geography and Environmental Science, Northumbria University, Newcastle Upon Tyne, UK

[20]Department of Geosciences, Virginia Tech, Blacksburg, VA, USA

[21]School of Earth Sciences and the SFI Research Centre in Applied Geosciences, University College Dublin, Dublin, Ireland

[22]Department of Environment, Geology, and Natural Resources, Ball State University, Munice, IN, USA

[23]Applied Structural Geology, Department of Earth Sciences, Indian Institute of Technology Kanpur, Kanpur, India

[24]Department of Marine and Coastal Sciences, Rutgers University, New Brunswick, NJ, USA

Corresponding author: Ashley M. Morris (ashley.m.morris@utah.edu)

Key Points:

- A dacitic unit was recovered in early Eocene sediments on the Vøring margin during International Ocean Discovery Program Expedition 396.
- The dacite was formed by upper crustal anatexis at 54.6 ± 1.1 Ma, postdating the Paleocene-Eocene Thermal Maximum.
- The dacite is evidence for a pre-breakup phase associated with significant continental lithospheric extension.

Abstract

While basaltic volcanism is dominate during rifting and continental breakup, felsic magmatism may also comprise important components of some rift margins. During International Ocean Discovery Program (IODP) Expedition 396 on the continental margin of Norway, a graphite-garnet-cordierite bearing dacitic, pyroclastic unit was recovered within early Eocene sediments on Mimir High (Site U1570), a marginal high on the Vøring transform margin. Here, we present a comprehensive textural, mineralogical, and petrological study of the dacite in order to assess its melting origin and emplacement. The major mineral phases (garnet, cordierite, quartz, plagioclase, alkali feldspar) are hosted in a fresh rhyolitic, highly vesicular, glassy matrix, locally mingled with sediments. The xenocrystic major element chemistry of garnet and cordierite, the presence of zircon inclusions with inherited cores, and thermobarometric calculations all support a crustal metapelite origin. While most magma-rich margin models favor crustal anatexis in the lower crust, thermobarometric calculations performed here show that the dacite was produced at upper-crustal depths (< 5 kbar) and high temperature (750–800 °C) with up to 3 wt% water content. In situ U-Pb analyses on zircon inclusions give a magmatic age of 54.6 ± 1.1 Ma, revealing the emplacement of the dacite post-dates the Paleocene-Eocene Thermal Maximum (PETM). Our results suggest that the opening of the North Atlantic was associated with a phase of low-pressure, high-temperature crustal melting at the onset of the main phase of magmatism.

Plain Language Summary

Fifty-six million years ago, the continents were beginning the final phase of their journey to their current configuration. This included the rifting and formation of the Northeast Atlantic Ocean, known in particular for the excess amounts of magmatic activity that accompanied continental breakup. The International Ocean Discovery Program organized Expedition 396 to collect volcanic and sedimentary rocks deposited during this time off the coast of present-day Norway to investigate the cause of the excess magmatism and its potential implications for the global climate. While sampling sediments on the expedition, an unexpected volcanic unit, a garnet-cordierite, glassy dacite, was recovered. To determine the origin and emplacement of this unit we combined multiple methods (petrography, stratigraphy, thermodynamic calculations, geochronology, in site compositional analyses) and showed that the unit was produced by

melting of the upper continental crust at depth during the rifting process and likely later emplaced as a pyroclastic flow in shallow water. Our results demonstrate that the rifting process in the Northeast Atlantic included a long and intense period of continental lithospheric thinning. This research provides evidence needed to reconstruct the evolution of the North Atlantic Ocean and associated magma production.

1 Introduction

The North Atlantic Igneous Province (NAIP) is an estimated 6–10×10^6 km^3 of magma that was emplaced during the Paleogene (64–35 Ma; Storey et al., 2007). Much of this volume was emplaced 56 to 54 million years ago (Ma), which coincides with the opening of the North Atlantic, which began around 56 Ma (Saunders et al., 2007; Horni et al., 2017; Westerhold et al. 2020; Planke et al., 2023a). In the NE Atlantic, on the mid-Norwegian rift margin, NAIP material is present as successions of voluminous extrusive basalt flows, including seaward dipping reflectors (SDRs), magmatic intrusions within the continental crust and associated sedimentary basins, and high-velocity bodies underlying the continent-ocean boundary (COB) at the base of the continental crust which, at least in the distal margin, are interpreted as a magmatic underplate (Fig. 1; Berndt et al., 2001; Mjelde et al., 2005; Planke et al. 2005; Planke et al., 2023a; Svensen et al.. 2004). Passive rift margins whose volume of magmatic production and volcanic activity cannot be explained by decompression melting of the sub-lithosphere at ambient mantle temperature, like the mid-Norwegian margin, are classified as excess magmatic margins (Lu & Huismans, 2001), or volcanic rifted margins.

Excess magmatism at volcanic margins was first attributed to active rifting (as opposed to passive rifting in non-volcanic margins; Celal Sengör & Burke, 1978). In a purely active model, a hot mantle (related, for example, to the presence of a mantle plume) thermally erodes the bottom of the lithosphere (Fleitout et al., 1896) and results in two stages of rifting: (1) flood basalt stage, coeval with very small crustal extension, and (2) a break-up stage associated with the volcanic margin formation (Courtillot et al., 1999). During active rifting, regional uplift predates and accompanies the volcanic margin development (e.g. Clift et al., 1998; White & Lovell, 1997). However, the purely active upwelling model is limited by evidence that many volcanic rifted margins are associated with regions that have been previously subjected to far-field extension (White & McKensie, 1989). This relationship suggests that prior extension may

facilitate volcanic activity and that deep mantle plumes may not be required to explain all cases of excess magmatism (e.g. Hill, 1991; White & McKensie, 1989). However, it is important to highlight that volcanic margins can also develop in areas that were not subjected to significant lithospheric stretching leading up to the flood basalt stage (e.g. in Afar; Courtillot et al. 1999). While accurate timing of the initiation and end of continental rifting, of the peak of magmatic activity, and of the main continental break-up phase is crucial to refine models of margin development, the causality and timing between rifting and excess magmatism is still poorly constrained.

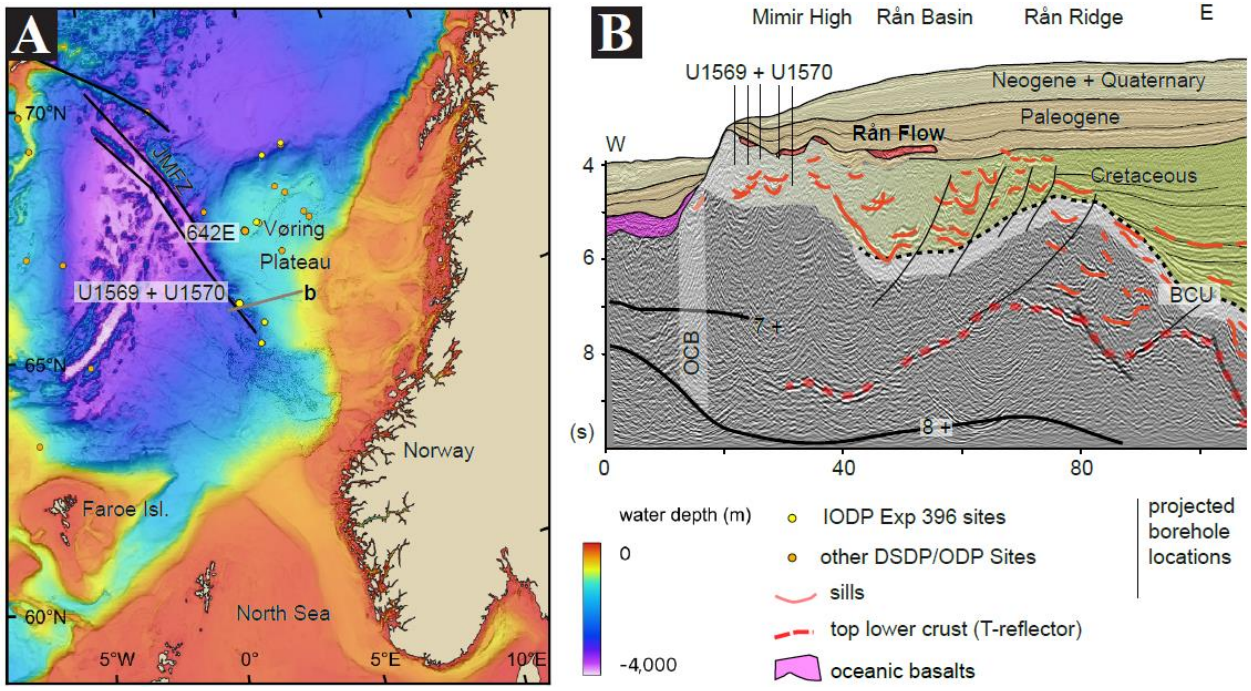

Figure 1. (a) Bathymetry map showing relative locations for IODP Expedition 396 (yellow circles), and for other DSDP/ODP sites (orange circles). The brown line shows the location of the seismic profile in (b). (b) Interpreted seismic section along Mimir High and the Rån Basin. The 7+ km/s and T-reflection (TR) are interpreted as the top of the lower crustal body (LCB), the 8+ km/s as the seismic Moho, and BCU, this Base Cretaceous Unconformity. Adapted from Abdelmalak et al. (2017).

During the recent International Ocean Discovery Program (IODP) Expedition 396, a dacitic unit was recovered in lower Eocene sediments deposited on the Mimir High (Fig. 1A; Planke et al., 2023b). Mimir High is a marginal high adjacent to the Vøring transform margin, the landward extension of the Jan Mayen Fracture Zone that segments the mid-Norwegian rift

margin. Dacite flows in oceanic or transitional regimes outside of volcanic arcs are unusual but not unique. For instance, they have been collected at several locations in the NAIP, including in Well 163/6-1A in the northern Rockall Trough (Morton et al., 1988a), in Well 209/3-1 in the Faroe-Shetland Basin (Kanaris-Sotiriou et al. 1993), in Hole 642E on the Vøring Plateau from Ocean Drilling Program (ODP) Leg 104 (Fig. 1; Eldholm et al., 1987; Viereck et al., 1988), and on the southeast Greenland margin (Larsen et al., 1995). Garnet and cordierite-bearing dacitic flows have also been reported in the Neogene Volcanic Province (NVP) in SE Spain that are associated with the opening of the Alborán Domain in the late Tertiary (Platt et al., 1998; Vissers et al., 1995). Dacitic flows have previously been interpreted as being products of crustal melting at various depths, with the units recovered in the NE Atlantic interpreted as produced in shallow magma chambers (Eldholm et al., 1989) and the units from SE Greenland as derived from magma differentiation and crustal contamination in the lower crust (e.g., Fitton et al., 1995).

Dacites previously collected in the NE Atlantic are peraluminous, suggesting they were generated through the melting or assimilation of pelitic sediments or metapelitic rocks. However, previously recovered units have experienced varying degrees of alteration (e.g., Abdelmalak et al., 2016; Morton et al., 1988) and, to our knowledge, no thermobarometric calculations were performed to constrain the origin of these rocks. Here, we use petrographic analyses, major and trace element compositions of mineral phases, in-situ U-Pb zircon dating, and thermodynamic modeling to discuss the petrogenesis and emplacement of the dacite in the context of the emplacement of the NAIP and explore the geodynamic implications for the development of the Vøring margin.

1.1 Geologic setting

Mimir High (Fig. 1) is a marginal high on the continent side of the continent-ocean boundary of the Vøring transform margin. This margin is characterized by diminished extrusive volcanism relative to the adjacent rifted margin segments of the Vøring and Møre basins (Berndt et al., 2001). The absence of basalt cover makes the Mimir High an exceptional place to study the stratigraphic successions and effects of sill intrusions (Planke et al., 2023). In fact, seismic interpretation suggests that the Mimir High was a depocenter during the Eocene, which makes it an ideal candidate for recovering expanded Paleocene–Eocene sedimentary sections. During Expedition 396, a transect of five boreholes was drilled along the Mimir High with the intention

of forming a composite ribbon core through most the Paleocene and Eocene strata (Fig. 2). In two of these boreholes (U1570A and D), the early Eocene sediments hosted a discrete (<10 m thick) glassy, garnet-cordierite-graphite dacitic igneous unit (Planke et al., 2023).

The dacite was recovered from between 146.84 and 151.96 meters below surface (mbsf) in Hole U1570A and between 100.75 and 110.91 mbsf in Hole U1570D (Fig. 2). The contact between the base of the dacite and dark gray and grayish-brown ash-rich siltstone was recovered in the cores from both boreholes. This basal contact is 8 and 9 m above the Paleocene–Eocene Thermal Maximum (PETM) interval in holes U1570D and U1570A, respectively (Vickers et al., 2023). Within both holes, the dacitic unit is observed as semi-discrete layers with local peperitic texture and mingling with dark, sand-rich silt with small (2–5 cm) intervals of silt and claystone between them (Fig. 2C). It is overlain by an early Eocene (Ypresian) age dark gray claystone with black ash and intervals of gray limestone. The top contact between the dacite and the early Eocene sediments was also recovered in Hole D (Fig. 2B). While this unit was not encountered in Hole U1569A, millimeter-size garnet grains were recovered in the core catcher of Section U1569A–35R collected at 315.66 mbsf. The location of this section is indicated by an open pink star in Figure 2F.

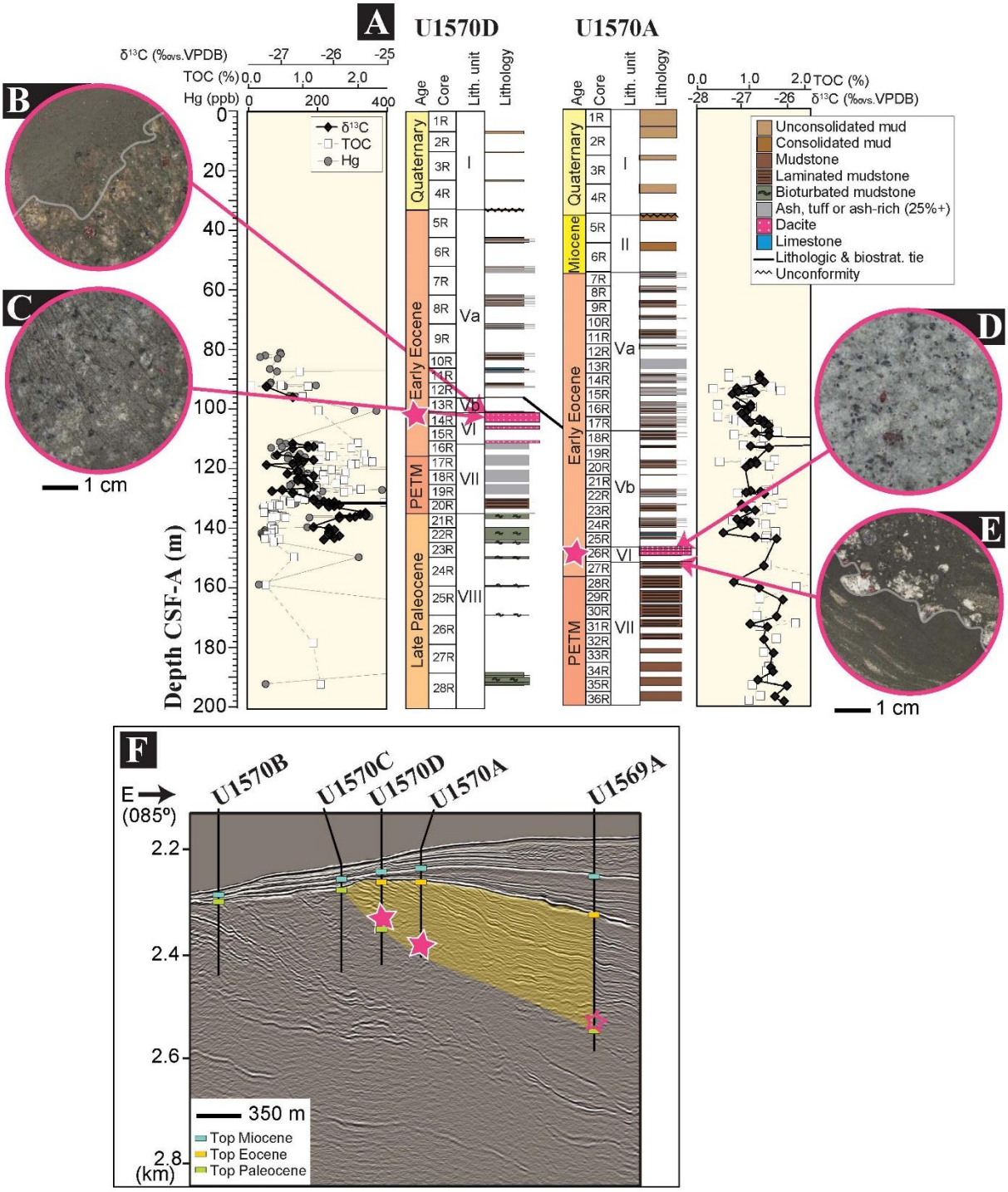

171

172 **Figure 2**. (a) Stratigraphic columns of the boreholes U1570D and U1570A cores modified from
173 Planke et al. (2023b) and associated TOC, Hg concentrations, and $\delta^{13}C_{org}$ measurements in the
174 sediments. The dacitic unit is represented in pink with white dots. Large circles show various
175 facies of the dacitic unit at the locations indicated by arrows in the stratigraphic column. (b)

Contact between the layered sediments and the dacite (sample 1570D-14R1-11-18, read as borehole U1570D, core 14, section 1 between 11 and 18 cm), (c) peperitic texture (sample 1570D-14R2-7-11), (d) a fresh, unmingled section of dacite (sample 1570A-26R2-51-54), and (e) basalt contact between the dacite and early Eocene sediment below (highlighted with a gray line; sample 1570A-27R1-9-13). The 1cm scale bar refers to all images of the core. (f) The interpreted seismic section at sites U1570 and U1569, adapted from Planke et al. (2023), showing the spatial relationship between the boreholes, geological epochs, and the locations of dacite recovery (pink stars); smaller open pink star is the recovery location of individual garnet grains at site U1569.

2 Methods

2.1 Bulk rock geochemical analyses

We analyzed two samples for major and trace element bulk rock concentrations; a representative fresh sample with little to no mixing with sediments (U1570A–26R2–51–54 cm; Fig. 2D) and a sample collected for being representative of mingling textures with the sediments (U1570D–14R2–7–11 cm; Fig. 2C). Sample U1570A-26R2-51-54 major element composition was done using Thermo Scientific ARL X-ray fluorescence (XRF) spectrometer at Institute of Geochemistry, Chinese Academy of Sciences. BHVO-2 and BCR-2 were used as secondary standards. Trace element concentrations were acquired using the Agilent-7900 inductively coupled plasma mass spectrometer (ICP-MS) at Institute of Oceanography, Chinese Academy of Sciences, following procedures of Chen et al. (2017). In brief, ~50 milligrams of the sample were dissolved with an acid mix of double distilled, concentrated HCl+HNO_3 and HF in a high-pressure bomb for 15 hours and then re-dissolved with distilled 20% HNO_3 for 2 hours until complete digestion/dissolution. BHVO-2 was used as a secondary standard. Analytical accuracy on secondary standards is better than 5% for all major elements and most trace elements, between 5% and 10% for Li, Cr, Mn, and Cu, and better than 15% for Be, Ti, V, Zn and Ta.

Sample U1570D-14R2-7-11 major element composition was analyzed using X-ray fluorescence spectrometry (Rigaku RIX3000) at Niigata University following the analytical method of Takahashi and Shuto (1997), with an optimization for ultramafic rocks. Trace element

concentrations were determined using a Yokogawa HP4500 ICP-MS at Niigata University, following the acid digestion method described in Senda et al. (2014). In brief, for each sample, 100 mg of material was weighed and placed in a Teflon vial and underwent step-by-step acid treatment with heating until the sample reached complete dissolution. The solution was finally diluted using HNO_3 and an internal standard (^{115}In) and was measured along with secondary standards (BHVO-2, W2a and JB2).Analytical accuracy on secondary standards is better than 5% for most elements, between 5 and 10% for Sc, Ga, Sr, Nb, Gd, Dy, Yb, Lu, Hf, and Pb, and 12% for Cs.

2.2 Sample selection for in situ analysis

Fourteen samples of the dacite unit were collected from both Holes U1570A and U1570D. Materials were sampled to include a range of apparent volcanic facies (undisturbed versus higher degrees of sediment mingling). Four thin sections (30 μm thick) were impregnated with blue epoxy to highlight the porosity. The remaining ten samples were cut, polished, and carbon-coated into thick sections (300–1000 μm thick) to minimize potential issues with the fragility of the sample and to facilitate laser ablation analyses.

2.3 Scanning electron microscopy and electron microprobe analysis

Scanning electron microscope (SEM) images presented in this study were collected using a JEOL JSM-IT300 at the Energy and Geoscience Institute (EGI) at the University of Utah. Major and minor element compositions were acquired using a Cameca SX100 electron microprobe at the University of Utah. A 15 keV beam voltage and 20 nA beam current were used for all analyses. Single spot measurements were used for mineral phases and glass using beam diameters of 5 μm and 10 μm, respectively, and 1–3 spots were analyzed on each large mineral phase. Sodium (Na) and potassium (K) were analyzed first, and a time-dependent intensity (TDI) correction was applied to correct the signal from devolatilization (Nielson & Sigurdsson, 1981; Siivola, 1969). Compositional profiles were also acquired across large (1–4 mm) garnet grains using a 5 μm beam diameter every ~120 μm (individual analysis locations within these profiles were adjusted to avoid cracks and inclusions). On-peak counting times were 10 s for major elements and 20 s for minor elements; half of the on-peak time was used on each of the high and low backgrounds. The following ASTIMEX reference standards were used, Rutile (Ti),

Chromite (Cr), Diopside (Ca), Albite (Al, Na, Si), Sanidine (K), Apatite (P), and Sphalerite (S). Additionally, we used synthetic Mn and a Ni olivine provided by George Rossman to calibrate Mn and Ni, and the USNM San Carlos olivine distributed by the Smithsonian Institute (USNM 111312/44) to calibrate Fe and Mg. Data were processed using the 'Probe for EMPA (v. 12.7.3)' software and the PAP procedure was used for data reduction (Pouchou & Pichoir, 1991). BHVO-2g and USNM San Carlos olivine 111312/44 were repeatedly analyzed as secondary standards during each analytical session to monitor drift on major and minor elements, but no additional corrections were applied.

2.4 Laser ablation inductively coupled plasma mass spectrometry

2.4.1 Trace element analysis of garnet, cordierite, and feldspars

Trace element concentrations in garnet, plagioclase, alkali feldspar, and cordierite were collected using laser ablation inductively coupled plasma mass spectrometry (LA-ICP-MS). Analyses were performed at the University of Utah on a Teledyne-Photon Machines Analyte Excite Excimer LA system attached to an Agilent 8900 ICP-MS. The laser carrier and the nebulizer gas flow were 1 L He/min (0.4 L/min cup +0.6 L/min cell and 1.1 L Ar/min, respectively). The first half of the analytical session was run using a fluence of 2.19 J/cm^2, which was later increased to 3.29 J/cm2 in an attempt to reduce shattering observed on quartz grains (see below). We used a laser repetition rate of 10 Hz. We used 40 μm spot analyses, with each analysis preceded by a cleaning shot. Acquisition times were about 50 s. To assess compositional variability, 1–5 analyses were performed per grain. NIST610 and NIST612 were measured every six unknown analyses for a (total n = 23) and used as primary standards for elements with concentrations higher and lower than 100 ppm, respectively. The Si contents, measured by electron microprobe, served as an internal standard. Each element signal was carefully monitored for spikes that may indicate the presence of cracks or inclusions; in this case, the analysis was discarded. We tested the accuracy of each measurement with BHVO-2G, which was acquired every 12 unknown analyses for a total of 10 analyses. Measured concentrations for BHVO-2G are compared with the GeoReM preferred values (Jochum et al. 2005); the relative errors on each trace element contents are reported in Table S1.

2.4.2 Trace element analysis of quartz

For quartz grains, we performed an additional analytical session with a fluence of 7.90 J/cm^2, a 5 Hz laser repetition rate, and pre-ablation cleaning spots for 85 μm single spot analyses. These conditions minimized the number of quartz grains shattered by the laser, providing 51 quartz analysis from 17 individual grains with good analytical signals. Elements analyzed in quartz are Ti, Li, Na, Al, P, K, Ge, Rb, Sr, Zr, and Ba. NIST610 was used as the primary reference material, measured once every five to eight quartz analyses for a total of 21 measurements. The data were processed by normalizing analytical peaks from the mass spectrometer by their ^{28}Si values and converted to ppm using the NIST610 standard values as calibration. NIST612 was used as a secondary standard. Comparison of the mean concentrations from 11 NIST612 analyses with the GeoReM preferred values (Jochum et al. 2011) shows that the relative error on the trace element contents in quartz is 6.7% for Ti and lies between 1.0 and 12.1% for the other analyzed elements (Table S1). We also performed six analyses on the reference material San Carlos Olivine NMNH 111312/42 and compared the data with data published in the literature (Lambart et al., 2022). The measured Ti concentration in olivine San Carlos reference material overlaps with the published values inside the two standard deviation (Table S1).

2.4.3 U-Pb zircon analyses

Twenty-five zircon crystals across two samples were located and imaged using backscattered electron and cathodoluminesence (CL) detectors. The BSE and CL images (Fig. S1) guided laser spot placements to minimize any mechanical mixing of chemically and/or isotopically distinct domains and to ensure an analysis of the full range of populations in each sample. Both U-Pb and trace element analyses were performed simultaneously for the two samples by Laser Ablation Split Stream (LASS; Kylander-Clark et al., 2013; Stearns et al., 2020) at the Petrochronology lab of the University of California Santa Barbara. The crystals were ablated using a Photon Machines/Teledyne 193 nm Excimer laser equipped with a two-volume Helex® stage (Eggins et al., 1998) and the ablated material was introduced via He carrier gas to the multi-collector ICP-MS and quadrupole (Q-MS) mass spectrometers to measure uranium, thorium, and lead isotopes and trace elements, respectively. The Nu Plasma multicollector measured ^{238}U, ^{235}U, ^{232}Th, ^{208}Pb, ^{207}Pb, ^{206}Pb, ^{204}Pb, ^{202}Hg and the Agilent 7700X quadrupole

292 measured Zr, Th, U, Si, P, Ti, V, Sr, Y, Nb, Mo, La, Ce, Pr, Nd, Sm, Eu, Gd, Tb, Dy, Ho, Er,
293 Tm, Yb, Lu, Hf, Ta, and W.

294 A total of 88 unknown analyses on the U1570 dacite's zircons were collected using a 12
295 μm spot size, a 5Hz laser operating frequency, and pre-ablation cleaning shots. A standard
296 sample bracketing method was used, and a series of primary and secondary reference materials
297 were measured, including GJ (608.5 Ma; Ehlou et al., 2006) and NIST612 as primary standards,
298 and 91500 (Weidenbeck et al., 2004), Aus (Kennedy et al., 2014), and Plešovice (337.13 Ma;
299 Sláma et al., 2008) as secondary standards. Comparison between the mean measured values and
300 the published values for trace elements are reported in Table S1.

301 2.5 MAGEMin thermodynamic calculations

302 The Mineral Assemblage Gibbs Energy Minimization (MAGEMin) thermodynamic
303 package (Riel et al. 2022) was used to calculate stability fields for minerals and their modal
304 proportions using the bulk composition of the dacite sample U1570-26R2-51-54 cm (Fig. 2D, 3)
305 for comparison with the phase assemblage observed in the samples. The MAGEMin program is
306 calibrated with the Holland et al. (2018) thermodynamic dataset and KNCFMASHTOCr
307 calculation system to perform single-point calculations at a given pressure, temperature, and
308 bulk-rock composition to find the most thermodynamically stable phase assemblage.
309 Pseudosections were computed using seven refinement levels and six cores for 0 to 6 kbar (1
310 kbar step size) and for 600 to 1000 °C (100 °C step size). Three pseudosections were calculated
311 to constrain the effect of water, using inputs of 1 wt%, 3 wt%, and 5 wt% H_2O.

312 2.6 Carbon isotopes and mercury concentration in sediments

313 We determined the total organic carbon (TOC) contents and stable carbon isotope ratios
314 ($\delta^{13}C_{org}$) of sediments around the dacitic unit by powdering and decalcifying samples using 1 M
315 HCl for 72 hours. A brief (c. 1 h) heating step at 50 °C during the acidification process was
316 included to remove any siderite that is occasionally present in these sediments. The samples were
317 then rinsed using deionized water, oven-dried at 50°C, and re-homogenized. We performed
318 analyses of a reconnaissance data set using a Thermo Fisher Scientific Flash Elemental Analyzer
319 coupled to a Thermo Fisher Scientific DeltaV Isotope Ratio Mass Spectrometer at the CLIPT
320 Lab, University of Oslo. Based on these initial results, we analyzed an expanded sample set for

TOC and $\delta^{13}C_{org}$ using a Thermo Finnigan DeltaPlus XP Mass Spectrometer at the School of Ocean and Earth Science and Technology (SOEST) at the University of Hawaii at Mānoa.

We performed mercury analyses at the University of Oxford (UK) using a Lumex 915Lab and a Lumex 915+ Portable Mercury Analyzer with a PYRO-915 pyrolyzer attached. Approximately 100 mg of oven-dried (40 ºC) and finely powdered sample was heated to >700 °C to volatilize the Hg present and Hg concentrations were determined via atomic absorption spectrometry. The instruments were calibrated using the NIST-SRM2587 (paint-contaminated soil) standard (290 ± 9 ppb) and long-term observations of the standards and samples showed that analytical errors for the Hg analyzers were ±6% (Frieling et al., 2023).

Total inorganic (TIC) and organic carbon (TOC) concentrations and thermal maturity of organic-carbon on the same sample powders as used for Hg were analyzed at the University of Oxford (UK) with a Vinci RockEval-6 device using standard procedures (Behar et al., 2001). For each sample, ~50 mg of dried powdered material was analyzed, and we assessed reproducibility with an in-house standard of homogenized sediment (~2.8% TOC, ~6% TIC). The standard deviation for TOC, TIC, hydrogen index and Tmax was ±1% of the measured value or better for the in-house standard (n = 6). The hydrogen index (HI) and oxygen index (OI) are defined as in Behar et al. (2001) where the mass of released hydrocarbons ("S2") and CO_2 ("S3") in mg is multiplied by 100 and divided by TOC to obtain HI and OI, respectively.

3 Results

3.1 Bulk rock composition

Major and trace element bulk rock compositions are reported in Table S2. Compositions obtained on both samples show similar major element compositions (Fig. 3A). The igneous samples from the two boreholes have a SiO_2 content of 66–70 wt%, an alkali (Na_2O+K_2O) content of 6.3 wt%, and an A/CNK (molar $Al_2O_3/(CaO+Na_2O+K_2O)$) aluminum saturation value of 1.5–1.6, classifying them as peraluminous dacite. Rare earth element (REE) diagrams from both samples (Fig. S2) also show similar enrichment in light-REE (LREE), with La_N/Sm_N ~3.1, and a moderate negative Eu anomaly ($Eu/Eu^* = Eu_N/(Sm_N*Gd_N)^{0.5}$ ~ 0.65). The two samples show slightly contrasted heavy-REE (HREE) depletion with a Sm_N/Yb_N ratios of 4.5 and 11.2 for the samples from U150D and U1570A, respectively.

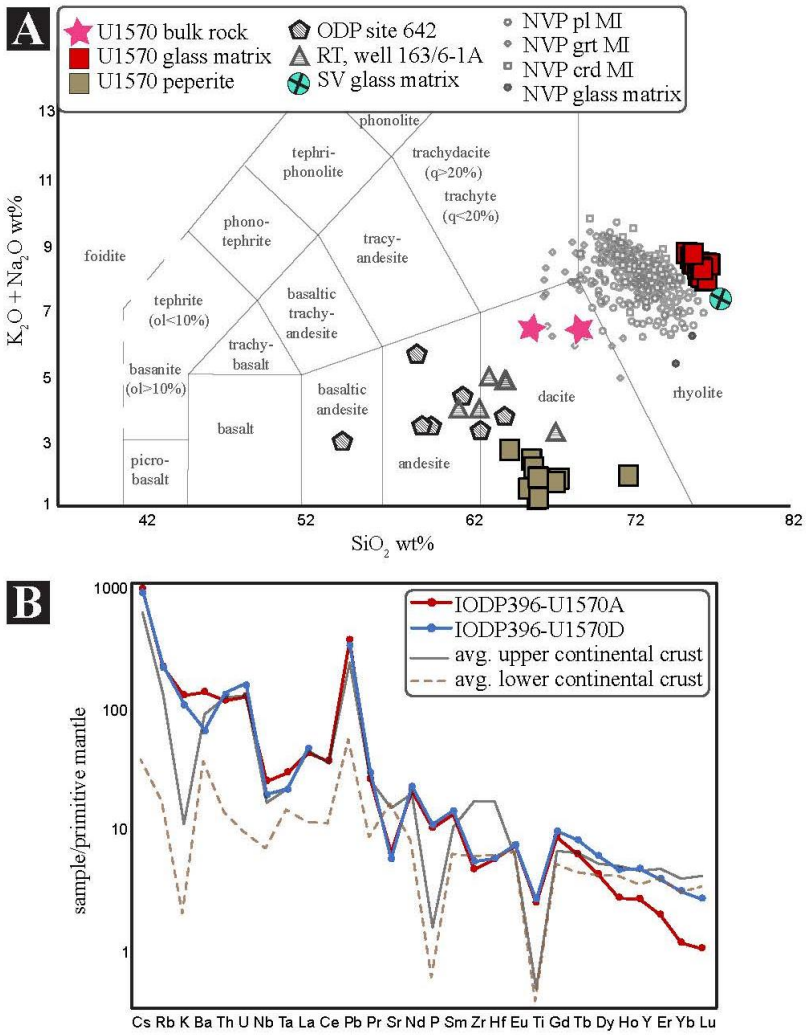

Figure 3. Total alkali-silica (TAS) diagram showing the bulk rock compositions of the U1570 dacite (pink stars); analyses performed on clear glass (red squares) are interpreted as fresh dacitic melt and analyses performed on the brown glass interpreted as the peperitic matrix (brown squares). For comparison, hatched pentagon symbols are the bulk rock compositions of the ODP Leg 104 in Hole 642E dacitic rocks (Eldholm et al., 1989), and hatched triangles represent dacites from the Rockall Trough (RT) Well 163/6-1 A (Morton et al., 1988). Small open symbols represent compositions of melt inclusions (MI) in various solid phases (pl=plagioclase; grt = garnet; crd = cordierite) from the El Hoyazo, Spain enclaves; filled gray circles are the matrix glass compositions for the El Hoyazo lavas (Álvarez-Valero et al., 2005, 2007). The blue, crossed circle represents the matrix glass compositions of the Shiveluch Volcano (SV; Humphreys et al., 2008). (B) Trace element bulk concentrations normalized to the primitive

mantle (Sun and McDonough, 1989) of the two dacite samples compare with the average values for the upper and lower continental crust (Rudnick and Gao, 2003).

3.2 Petrography and microstructures

We estimated phase proportions using the GeoBalance mass balance calculation spreadsheet based on a least squares problem (Li et al., 2020) for inputs of the mean bulk rock composition, and the major element compositions obtained on solid phases and glass. The dacite is composed of 67 ± 12 wt% glass with ~12 wt% cordierite, ~7 wt% plagioclase, ~5 wt% quartz, ~2 wt% garnet, ~1 wt% alkali feldspar, ~1 wt% ilmenite, ~0.5 wt% apatite, and less than 6 wt% of other accessory minerals (e.g., pyrite, zircon) and products of alteration (e.g., kaolinite).

The most abundant solid phase, cordierite, occurs as <1 mm to 4 mm large grains. These are subhedral, with distinctive void space around the edges and along cracks (Fig. 4). Subhedral almandine garnets were also identified in most samples. Both garnet and cordierite grains contain abundant solid (ilmenite, pyrite, apatite, zircon) and melt inclusions (Fig. S3). Garnet is also present in inclusion in cordierite (Fig. 5C). Large (2–6 mm) quartz grains are euhedral to subhedral, often with very few or no inclusions (Fig. 4). Garnet, cordierite, and quartz are also often highly fragmented (Figs. 4 and 5). Finally, plagioclase grains are subhedral with few inclusions, sometimes with evidence of dissolution at the margins (Fig. 4A) and alkali feldspars are mostly anhedral and sometimes contain large melt inclusions and embayments (Fig. 4E). Smaller (<1mm) mineral phases disseminated in the samples include ilmenite, pyrite, apatite, kaolinite, and graphite. Graphite is also observed both as a monomineral phase as thin deposits on larger grains (Fig. 5). The matrix is rhyolitic glass (~77 wt% SiO_2; Fig. 3) in ash-sized glass shards and micro-pumices. Mix domains exist where dark sand and silt are mingled within the crystal-rich ash with a preserved grain structure (Figs. 4, 5).

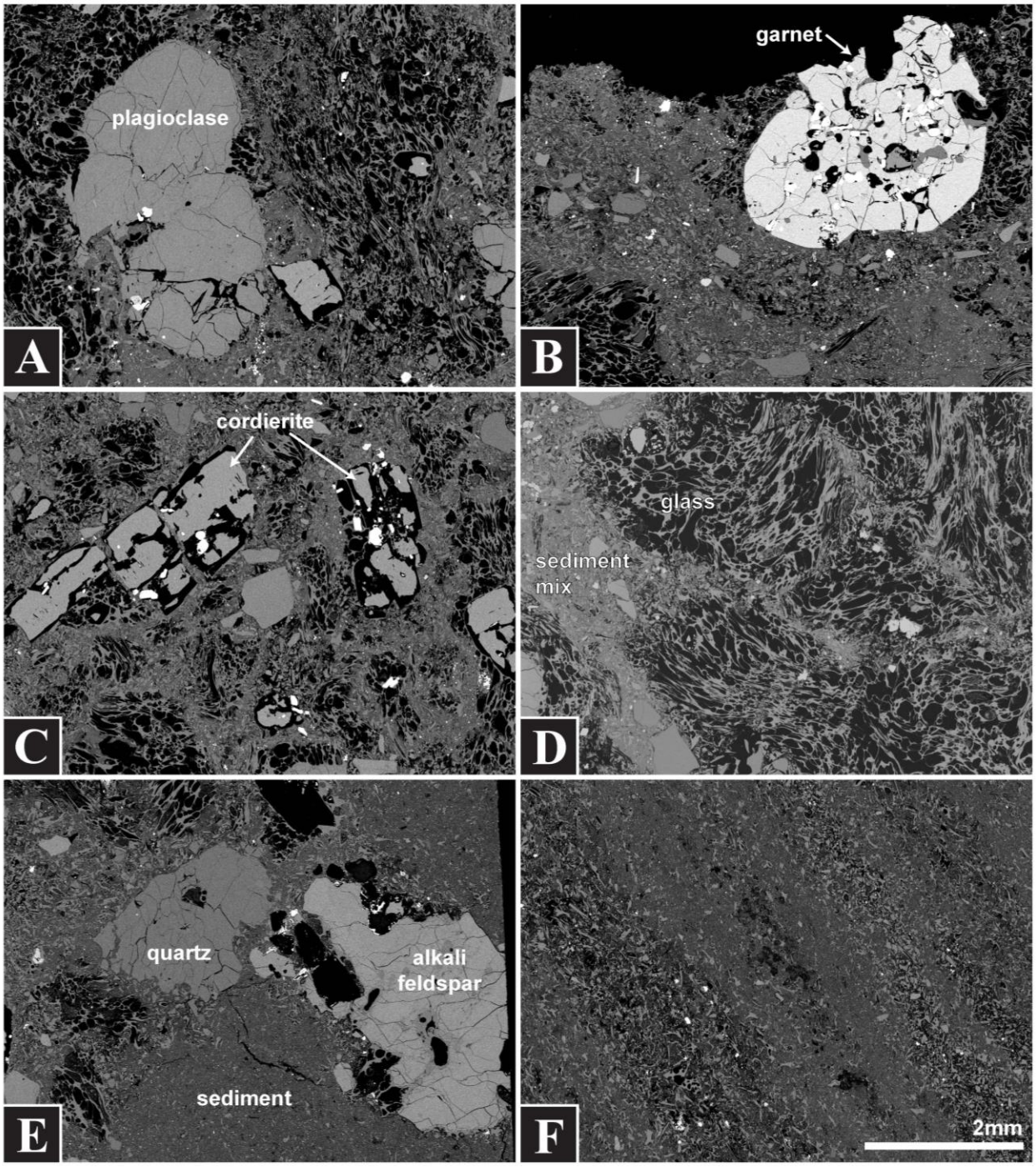

Figure 4. SEM-BSE images highlighting the various textures observed in the dacitic unit. (a) Plagioclase grain showing dissolution texture on the rim (sample U1570A-26R2-4). (b) Inclusion-rich garnet grain (sample U1570A-26R2-4). (c) Subhedral fractured cordierite grains surrounded by void space (sample U1570A-26R2-4). (d) Texture showing mingling between the vesicular glass and the sediments (sample U1570D-15R1-36). (e) Grains on the basal contact of

391 the dacite with sediments (sample U1570A-27R1-10). (f) Preserved layering of sediments less
392 than a centimeter away from the basal contact of the dacite (sample U1570A-27R1-10). All
393 images have the same scale.

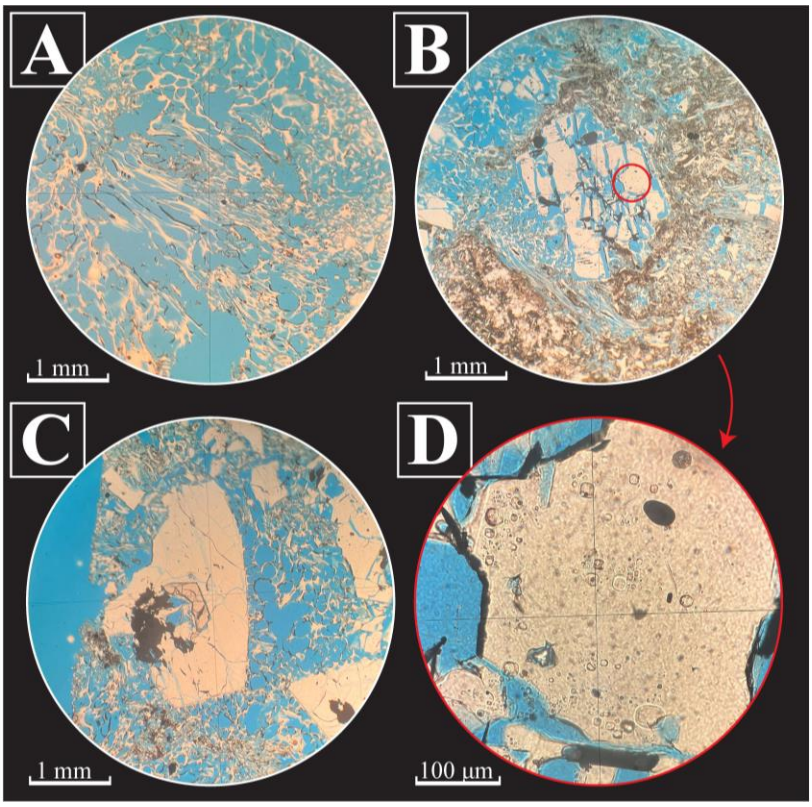

394

395 **Figure 5**. Petrographic images of samples impregnated with blue epoxy to highlight textures and
396 porosity. (a) Example of pumiceous glass texture with elongated and folded vesicles (sample
397 U1570D-14R3-8). (b) Cordierite grain showing fragmented texture with associated graphite
398 (sample U1570A-26R1-26). (c) Garnet and graphite in inclusion in a cordierite grain (sample
399 U1570A-26R2-44). (d) Melt inclusions in cordierite grain from (b).

400 ## 3.3 Mineral chemistry

401 ### *3.3.1 Major and minor elements*

402 The twelve garnets analyzed are all Fe-rich, almandine-pyrope solid solution (77–85%
403 Alm, 7–15% Py; Fig. 6A; Table 1). They are MnO- and CaO-poor with fractions of spessartine
404 (XSpss) and grossular (XGrs) of 0.040 ±0.003 (1σ) and 0.03 ±0.01 (1σ), respectively (Fig. 6B).
405 The garnets show a relatively constant Mg# (molar Mg/[Mg + Fe]x100) = 12.7% ± 0.7% (1σ).

Garnet crystals from samples across boreholes show no significant variations in major element concentrations. Ten of these garnets were large enough to acquire compositional profiles. There is no systematic zonation in the grains, and the compositional variability is limited with 0.05 ±0.04 wt% FeO and 0.21 ±0.05 wt% MnO mean relative variability per grain (Fig. S4).

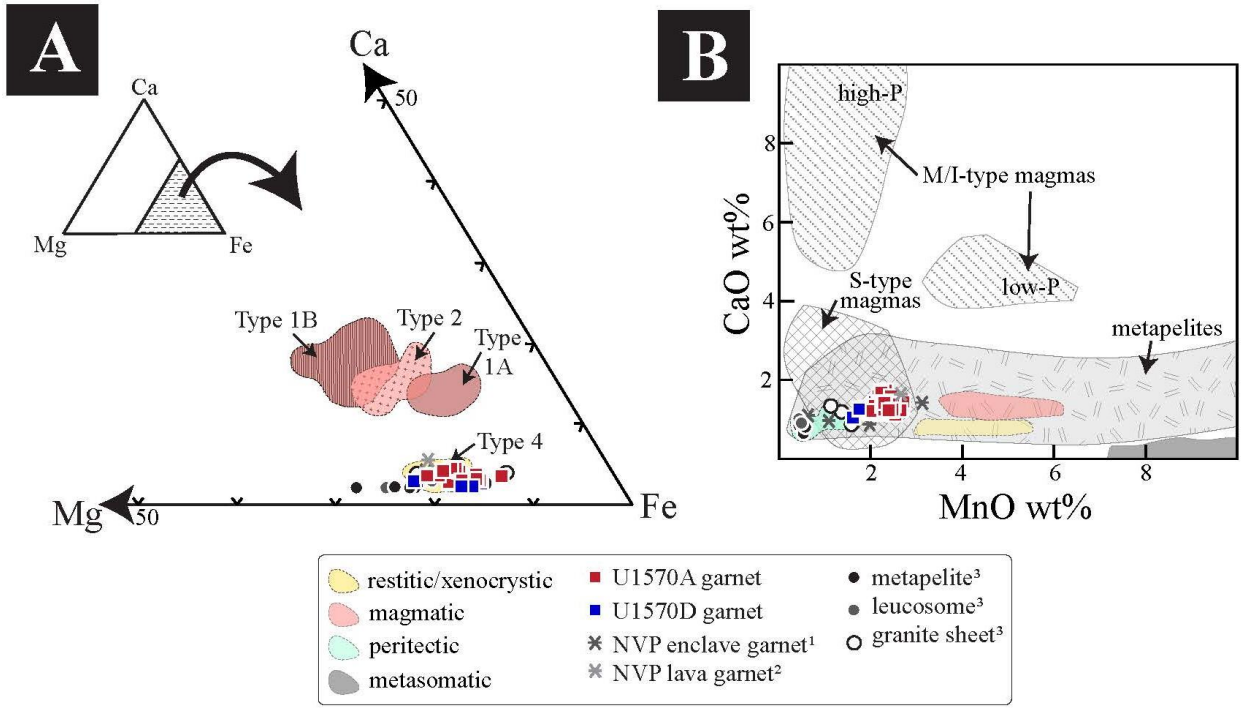

Figure 6. (a) Mg-Ca-Fe ternary plot (Harangi *et al.*, 2001) with the compositions of garnets analyzed in enclaves found in the Neogene Volcanic Province (gray asterisks; Álvarez-Valero & Waters, 2010) and as separated grains in the associated lavas (black asterisks; Hiwatashi et al., 2021) and in Mkhondo Valley Metamorphic Suite rocks separated by the three stages of "selective peritectic phase entrainment": 1) metapelite (black filled circles), 2) leucosome (gray circles), and granite sheet (black open circles; Taylor & Stevens, 2010). (b) CaO vs. MnO wt% plot; colored fields represent different types of garnet adapted from Khedr *et al.* (2022) and gray, patterned fields represent garnets from different sources adapted from Harangi *et al.* (2001). On both plots, restitic and xenocrystic-type garnet compositions are represented by yellow fields and magmatic garnet compositions are represented by light red fields. In (b), peritectic-type garnets are represented by the light blue field and metasomatic garnets by the solid dark gray field. U1570A (red squares) and U1570D (blue squares) garnet compositions are plotted. See text for details.

Table 1. Major element summary for major phases in the dacite samples.

	garnet *n = 229*		**cordierite** *n = 94*		**plagioclase** *n = 60*		**alkali feldspar** *n = 26*		**quartz** *n = 61*		**ilmenite** *n = 62*		**kaolinite** *n = 15*		**apatite** *n = 5*		**glass** *n = 35*	
	< >	*1σ*	< >	*1σ*	< >	*1σ*	< >	*1σ*	< >	*1σ*	< >	*1σ*	< >	*1σ*	< >	*1σ*	< >	*1σ*
SiO_2	35.89	0.69	47.22	0.50	56.22	1.58	65.12	0.45	99.84	0.05	0.21	0.31	78.84	2.10	0.00	0.00	76.60	0.33
TiO_2	0.05	0.07	0.01	0.01	0.02	0.01	0.03	0.01	0.03	0.02	51.45	0.66	0.14	0.04	0.04	0.01	0.12	0.01
Al_2O_3	21.40	0.42	33.09	0.51	27.72	1.14	19.78	0.57	0.08	0.01	0.15	0.03	13.23	0.23	0.01	0.00	13.05	0.10
FeO	36.66	0.99	13.83	0.39	0.10	0.03	0.03	0.02	0.03	0.02	47.08	0.66	2.03	0.21	1.61	0.16	1.45	0.24
MnO	1.78	0.13	0.23	0.03	0.02	0.01	0.01	0.01	0.01	0.01	0.46	0.04	0.05	0.01	0.21	0.08	0.03	0.02
MgO	2.99	0.14	5.38	0.12	0.00	0.00	0.00	0.00	0.01	0.02	0.67	0.02	0.09	0.02	0.23	0.01	0.09	0.01
CaO	1.05	0.08	0.01	0.01	9.08	1.23	0.09	0.05	0.01	0.00	0.01	0.01	0.31	0.04	54.91	1.46	0.32	0.02
Na_2O	0.02	0.04	0.08	0.02	6.10	0.59	3.20	0.07	0.01	0.02	0.02	0.02	2.26	0.82	0.00	0.00	3.28	0.15
K_2O	0.01	0.04	0.13	0.01	0.65	0.18	11.67	0.22	0.01	0.01	0.01	0.01	2.76	1.60	0.01	0.00	5.04	0.20
Total	100.74	3.53	100.65	0.81	0.11	0.02	98.60	1.23	99.26	1.13	101.36	1.61	93.55	3.33	98.25	0.71	92.37	2.64
	(12 oxygens)		(18 oxygens)		(8 oxygens)		(8 oxygens)		(2 oxygens)		(3 oxygens)		(9 oxygens)		(4 oxygens)			
Si	3.3477	0.0592	5.9169	0.0408	2.9955	0.0622	3.3588	0.1580	0.9991	0.0002	0.0010	0.0047	4.0754	0.0295	0.0000	0.0000		
Ti	0.0034	0.0036	0.0009	0.0009	0.0006	0.0005	0.0006	0.0010	0.0002	0.0001	0.9305	0.0099	0.0053	0.0014	0.0004	0.0005		
Al	1.1759	0.0248	2.4430	0.0461	0.8685	0.0440	0.6306	0.0966	0.0005	0.0001	0.0027	0.0020	0.4032	0.0126	0.0001	0.0001		
Fe	2.8527	0.1032	1.4536	0.0558	0.0107	0.0473	0.0388	0.1389	0.0002	0.0002	1.1041	0.0184	0.0880	0.0091	0.0500	0.0042		
Mn	0.1400	0.0107	0.0247	0.0035	0.0006	0.0006	0.0007	0.0023	0.0001	0.0001	0.0107	0.0010	0.0020	0.0006	0.0064	0.0025		
Mg	0.4157	0.0203	1.0032	0.0396	0.0001	0.0003	0.0254	0.0948	0.0001	0.0002	0.0120	0.0016	0.0061	0.0028	0.0127	0.0004		
Ca	0.1085	0.0446	0.0014	0.0010	0.5170	0.0749	0.0040	0.0034	0.0000	0.0000	0.0001	0.0005	0.0174	0.0020	2.1841	0.0226		
Na	0.0016	0.0048	0.0119	0.0255	0.3155	0.0282	0.1524	0.0337	0.0001	0.0001	0.0006	0.0013	0.1140	0.0425	0.0000	0.0000		
K	0.0005	0.0028	0.0103	0.0021	0.0221	0.0059	0.3627	0.0916	0.0000	0.0000	0.0003	0.0008	0.0920	0.0549	0.0002	0.0001		
% Alm	81.11	1.21																
% Spss	3.99	0.34																
% Grs	3.07	1.10																
% Py	11.83	0.69																

Oxides concentrations are given as wt. % and elemental concentrations are given as molar fractions. Molar fractions are normalized to 12, 18, 8, and 3 for garnet, cordierite, feldspars, and ilmenite, respectively. Values are the averages of all the measured grains (< >) and the associated standard deviation (1σ). Garnet solid solution end-member proportions are also provided: Alm = almandine, Spss = spessartine, Grs = grossular, Py = Pyrope. Individual analyses are provided in Table S3.

The cordierite crystals have an Mg# = 40.8 ±1.6. They have low abundances of Na and K with total alkali (Na + K) molar fraction of 0.02 ±0.03 (Fig. 7). Plagioclase grains classify as labradorite, with 60.2% anorthite and 37.2% albite. Alkali feldspars are 46–72% orthoclase and 28–46% albite (Fig. S5A). No significant variability across samples or boreholes is observed. All ilmenite crystals are mostly pure ilmenite with a ≤ 0.01% pyrophanite ($MnTiO_3$) component (Table 1).

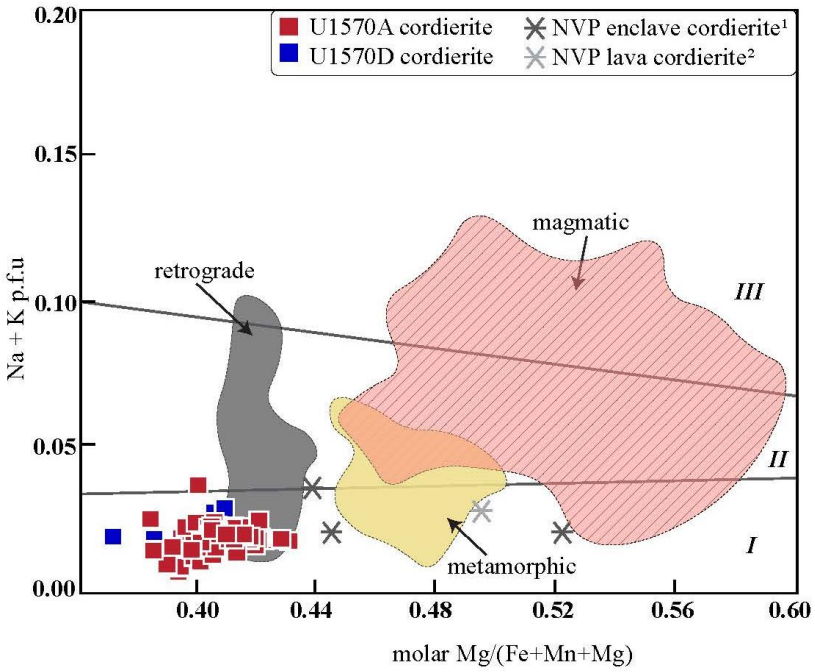

Figure 7. (Na + K) p.f.u (assuming 18 Oxygens) vs. molar Mg/(Fe+Mn+Mg) ratios of cordierite grains from our study: samples from U1570A (red squares) and U1570D (blue squares). Cordierite compositions from enclaves (gray asterisks; Álvarez-Valero & Waters, 2010) and separate grains in lavas (black asterisk; Hiwatashi et al., 2021) in the Neogene Volcanic Province volcanic rocks are shown for comparison. Adapted from Pereira and Bea (1994), the magmatic (red), metamorphic (yellow), and retrograde (gray) fields were classified by petrographic textures of cordierite grains. Solid lines define fields based on the chemical compositions of metamorphic (*I*), anatectic (*II*), and magmatic (*III*) cordierite grains.

3.3.2 Trace elements

Chondrite-normalized (McDonough & Sun, 1995) garnet REE patterns show notable LREE depletion (Ce_N/Yb_N = 0.0001-0.0009), with strong negative Eu anomalies (Eu/Eu* =

0.01–0.04; Fig. 8). HREE slopes are variable, measured by Lu_N/Gd_N ratios ranging from 0.1–20.2 with a difference up to Lu_N/Gd_N = 16.9 within a single grain (Fig. S6). While some garnets show core-rim variation with steeper HREE slopes in their cores (Fig. S6), others show more complex patterns. Using the mathematical approach described by Anenburg and Williams (2022), no clear distinction can be made between the garnet grains. Garnet concentrates Sc, Ti, V, and Cr relative to other phases (Table 2). Y concentrations are highly heterogeneous, ranging from 170 to 1323 ppm, with intragranular variability as high as 858 ppm and are generally positively correlated with HREE concentrations.

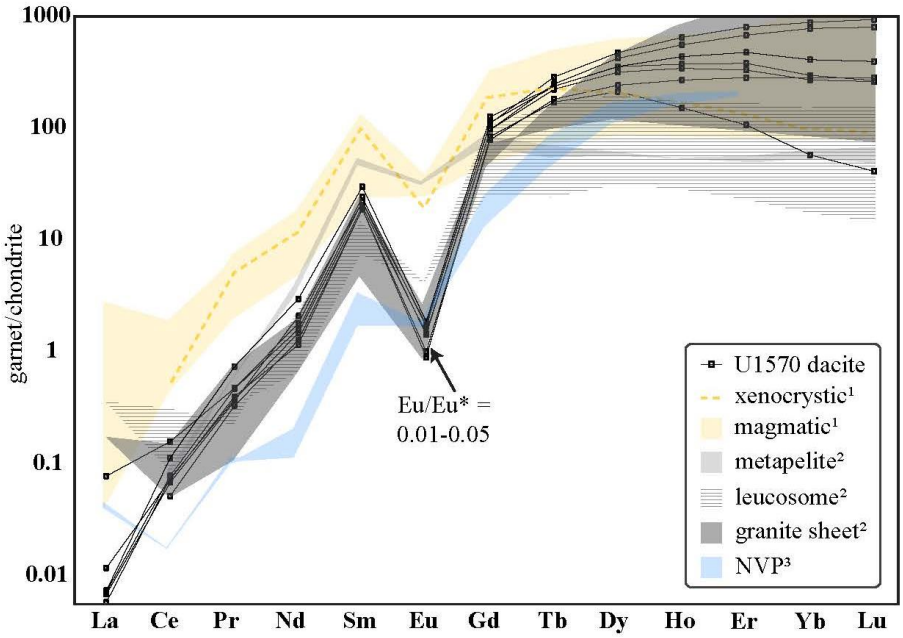

Figure 8. Chondrite-normalized (McDonough & Sun, 1995) garnet REE concentration diagrams. The black lines represent the mean composition of individual garnet grains analyzed in our samples (individual analyses on each garnet are plotted in Fig. S6B), compared with magmatic (yellow field) and xenocrystic (yellow, dashed line) garnets from Northern Pannonian Basin calc-alkaline volcanic rocks. The gray fields represent REE concentrations of garnets from three representative stages of "selective peritectic phase entrainment", (1) the metapelite garnets (light solid gray), (2) leucosome garnets (horizontal gray lines), and (3) granite sheet garnets (solid dark gray. Neogene Volcanic Province volcanic rock garnets are represented by the blue field. Subscripts 1, 2, and 3 in the legend correspond to Harangi et al. (2001), Taylor & Stevens (2010), and Álvarez-Valero & Waters (2010), respectively.

Table 2. Mean trace element concentrations (μg/kg) for major solid phases in the dacite.

	garnet	±	cordierite	±	plagioclase	±	alkali feldspar	±	quartz	±	zircon	±
	n = 25		*n = 28*		*n = 22*		*n = 18*		*n = 62*		*n = 88*	
Li									42	8		
Sc	240	112	1.12	0.74	0.16	1.17	0.8	3.0				
Ti	194	50	32.2	15.1	76.97	17.88	108	24	148	41	15	43
V	616	110	6.76	1.45	0.99	0.33	0.2	2.0			3	17
Cr	641	356	2.01	2.12	3.30	2.86	0.4	13.4				
Co	37.4	1.2	26.1	1.3	0.20	0.72	0.32	1.47				
Zn	178	13	277	18	8.55	13.86	6.7	27.4				
Ga	13.3	1.1	47.3	3.1	34.82	3.59	16.71	3.31				
Ge	11.6	2.3	0.50	2.58	1.47	2.51	1	8	1.00	0.36		
Rb									0.21	0.43		
Sr	0.04	0.03	0.07	0.13	662	72	472	68	0.29	0.55	0.9	1.45
Y	606	268	0.02	0.05	2.30	0.53	0.14	0.16			1650	686
Zr	23.9	10.0	0.30	1.07	0.06	0.13	0.00	0.27	0.31	0.59		
Ba									0.44	0.88		
La	0.01	0.02	0.01	0.04	33.67	7.56	4.48	0.75			5	33
Ce	0.06	0.04	0.03	0.11	59.8	13.6	4.23	0.72			19	78
Pr	0.05	0.02	0.00	0.01	5.66	1.44	0.26	0.10			1	5.7
Nd	0.88	0.41	0.01	0.03	19.1	5.5	0.48	0.24			5	21
Sm	3.57	0.81	0.01	0.02	3.10	0.69	0.06	0.09			7	7
Eu	0.09	0.04	0.00	0.00	6.02	0.60	5.08	0.84			0.52	0.74
Gd	21.7	4.5	0.03	0.06	1.83	0.54	0.02	0.07			43	17
Tb	8.92	1.84	0.00	0.00	0.20	0.06					14.09	4.84
Dy	91.3	28.1	0.01	0.02	0.81	0.31					162	62
Ho	24.0	12.1	0.00	0.01	0.10	0.05					56.43	24.1
Er	77.5	55.2	0.00	0.01	0.17	0.11					242	117
Yb	78.4	79.6	0.00	0.00	0.05	0.06					432	244
Lu	11.8	13.5	0.00	0.00	0.01	0.03					87	50
Hf	0.46	0.18	0.01	0.04	0.00	0.07	0.02	0.05			11094	1200
Ta	0.01	0.00	0.00	0.02	0.00	0.00	0.07	0.04			0.73	0.97
Th	0.01	0.00	0.01	0.04	0.01	0.02	0.01	0.04			118	354
U	0.01	0.01	0.01	0.03	0.00	0.02					271	275

Values are the averages of all the measured grains (< >) and the associated standard deviation (1σ). Individual analyses are reported in Table S4.

Trace element analysis for cordierite crystals shows they are very REE-depleted (ΣREE_N < 1.5 ppm). Cordierites are Zn-enriched and Sr-depleted relative to other phases (Zn = 277 ± 18 ppm, Sr = 0.07 ± 0.13 ppm; Table 2). Plagioclase is LREE-enriched relative to HREE (La_N/Sm_N = 5.6–12.0). They are relatively enriched in Sr, Ti, and Cr with small positive Eu anomalies (Eu/Eu* = 5.0–10.0; Fig. S5B; Table 2). In comparison, alkali feldspars are significantly more LREE-depleted, but present more fractionated patterns (La_N/Sm_N = 10.1–125.0). They also

concentrate more Ti and less Sr than plagioclase and have strong positive Eu anomalies (Eu/Eu* 189.2–521.0; Fig. S5B; Table 2).

3.4 U-Pb zircon ages

Zircon grains have only been observed as inclusions in garnet and cordierite and are dominantly subhedral with rare euhedral crystals. Many of the zircons are fractured and range from 10 to 100μm in diameter (Fig. 9A). Zircon analyses were plotted on a Tera-Wasserburg concordia plot ($^{238}U/^{206}Pb$ vs. $^{207}Pb/^{206}Pb$; Tera & Wasserburg, 1972) in the IsoplotR toolbox (Vermeesch, 2018). The data define a ternary mixing field in Tera-Wasserburg space with the endmembers interpreted as (1) dominant younger populations, with a subset of concordant analyses and (2) sparse older inherited population of zircon. Non-anchored, uncertainty-weighted linear regression (i.e. model-1 fit) of the young, concordant analyses with the array of young analyses containing variable amounts of common Pb (population 1, Fig. 9B) yielded an initial lead composition of 0.79 ± 0.1 ($^{207}Pb/^{206}Pb$) and lower intercept of 54.8 ± 1.1 Ma (MSWD = 1.7). The lower intercept of a linear regression anchored to Stacey-Kramer initial Pb value of 0.85 also yielded a 54.8 ± 1.1 Ma (mean square weighted deviation, MSWD = 1.7; Ludwig, 1997; Andersen, 2002; Chew et al., 2014). Spot dates were calculated using the Stacey-Kramer anchored ^{207}Pb correction (Fig. 9A). Analyses with $^{238}U/^{206}Pb$ less than 105 and concordance outside of 0.9–1.05 were excluded from the weighted mean calculation. The weighted mean date of 54.6 ± 1.1 Ma, calculated using concordant analyses from population 1, is interpreted as the magmatic age of the dacite. The analyses interpreted as inherited (#2 above) yielded spot dates ranging from 61–2500 Ma (Fig. S7).

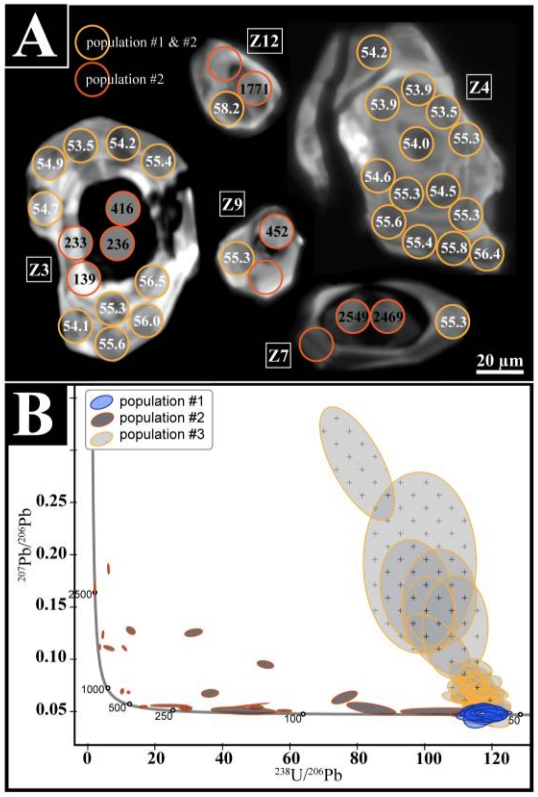

Figure 9. (a) Representative cathodoluminescence images of zircon grains from sample U1570A-26R-2-4. Circles represent LA-ICP-MS analysis locations, and the numbers are the calculated spot age for that analysis. Empty circles show spot ages that did not fall on the regression from the weighted average and were too discordant (concordance >0.9) to calculate ages. Populations #1 and #3 (magmatic) and #2 (inherited) are represented in yellow and orange, respectively. (b) U-Pb isotope results for zircon on Tera-Wasserburg Concordia plot. Only analyses in blue were used to calculate the formation age of the dacite (see text for details). Population #1 includes samples that fit a regression from the weighted average to the expected original $^{207}Pb/^{206}Pb$ and represent magmatic young zircons. Samples that do not fit the regression are included in population #2, representing older inherited zircon.

3.5 Sedimentary mercury concentration and organic carbon maturation data

The stable carbon isotope analyses of bulk organic matter ($\delta^{13}C_{org}$), total organic carbon (TOC) and mercury (Hg) contents in the sediments collected in borehole U1570A and U1570D

are plotted in Figure 2 and reported in Tables S5 and S6. Sedimentary mercury concentrations are ~190 ppb (mean) for the sediments analyzed for U1570D (81.23 meters below surface, mbsf, CSF-A to 192.28 mbsf). Two strongly Hg enriched samples (> 1 ppm; 87.25 and 172.4 mbsf) were found but these occur 10s of meters from the dacitic unit. For other samples, mercury concentrations are above average shale values (~ 62 ppb, Grasby et al., 2019) throughout the succession but no clear trends in Hg concentration were observed towards the dacite unit.

Organic-carbon maturation data obtained through RockEval analyses indicates the organic-matter preserved in the sediments is immature; Tmax averages ~ 405 ºC. RockEval parameters HI (mean ~50) and OI (mean ~130) signal a dominant terrestrial organic-matter composition. Total organic carbon concentration measurements yielded ~0.6 wt% for the Paleocene interval and ~1.1 wt% for the lower Eocene and, similar to Hg concentrations, none of the RockEval parameters (TOC, HI, OI, Tmax) show trends towards the dacite unit.

4 Interpretation of texture and mineral chemistry of garnet and cordierite

Our samples contain mineral phases commonly found in crustal metapelites and restites, particularly garnet and cordierite produced during crustal anatexis (Fig. 4, 5; Harley & Carrington, 2001; Vry et al., 1990; White & Chappell, 1977; Stevens et al., 1995, 2007; Weinburg & Hassalova, 2015). In this context, these minerals could be (1) liquidus phases produced during the crystallization of a magma as phenocrysts; (2) disseminated xenocrysts from the original protolith; or (3) peritectic phases entrained during magma transport. A magmatic chemical signature would indicate they are liquidus phases, while a metamorphic signature would indicate they are either disseminated xenocrysts or peritectic phases which preserve the chemistry of the protolith. Below, we use several proxies to distinguish magmatic and metamorphic major and trace element compositions of garnet and cordierite.

Harangi et al. 2001 and Bach et al. (2012) presented similar classifications based on the Ca, Mg, and Fe (±Mn) components of the garnet solid solution. Both studies show that magmatic garnets are systematically more enriched in grossular than metamorphic garnets (Fig. 6). Garnet compositions in our study are relatively depleted in grossular, overlapping the compositions of xenocrystic garnets described in Harangi et al. (2001) and plotting near metamorphic garnet

compositions in Bach et al. (2012)'s classification, but with a more significant almandine-spessartine enrichment in comparison to the garnet compositions reported in their study. According to the classification defined by Pereira and Bea (1994) based on alkali content and Mg# (= molar Mg / [Mg+Fe+Mn]), the cordierite grains in our samples also show a metamorphic major element signature (Fig. 7).

Harangi et al. (2001) did not report trace element analyses on pure xenocrystic garnets but rather on composite garnets, interpreted as xenocryst cores surrounded by magmatic rims (Fig. 8). Both the magmatic and composite garnets from their study show REE patterns similar to those observed in our samples, displaying substantial LREE depletion and variable HREE slope. While none of them have negative Eu anomalies as prominent as those observed in the garnet grains from the Site U1570 dacite, the Eu anomalies for the xenocrystic cores of composite garnets (Eu/Eu* = 0.14) are stronger than those reported for the magmatic garnets (Eu/Eu* = 0.17–0.68; Fig. 8). Harangi et al. (2001) also reported depleted Y (277 ppm) and enriched Zr and Hf (178 and 2.75 ppm, respectively) for the xenocrystic core compositions relative to magmatic compositions. In comparison, garnets from our study have more variable Y contents (170–1323 ppm) and lower Zr and Hf concentrations (9–47 and 0.20–0.84 ppm, respectively; Table 2). However, trace elements concentrations of magmatic garnets reported in Bach et al. (2012) show Y, Zr, and Hf variability covering the entire range of those presented for magmatic and xenocrystic garnets in Harangi et al. (2001), indicating that these elements are not reliable proxies for garnet origin.

In their study of mid-crustal anatectites from the Mkhondo Valley Metamorphic Suite, Swaziland, Taylor and Stevens (2010) outlined how garnet can undergo several stages of entrainment that result in modifications to both their major and trace element compositions (Fig. 10). By analyzing almandine garnet from metapelites, leucosomes, and granite sheets, they proposed these garnets represent a sequence of processes related to "selective peritectic phase entrainment," in which only solid peritectic products become entrained by associated melts (Stevens et al., 2007). This model provides a mechanism to produce hot, water-undersaturated, granitic magmas. Preferential entrainment of garnet and ilmenite during high-temperature, incongruent, fluid-absent melting of biotite metapelites results in an increase in A/CNK, Mg#, and Ca content and a decrease in Si and K in the magma.

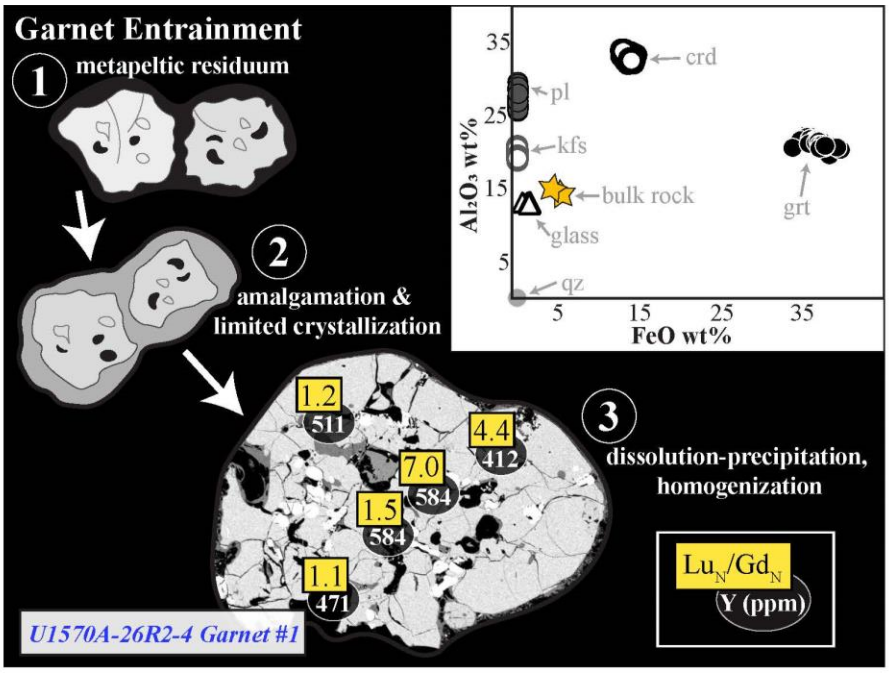

Figure 10. Summary of thermobarometric calculations. The gray dashed line represents the mean temperature calculated for Ti concentration in quartz using Wark and Watson (2006)'s original TitaniQ thermometer with no pressure correction (standard deviation represented by the gray field). Black circles represent the pressure-dependent thermometer for Ti concentration in quartz for Huang and Audétat (2012). For comparison the pressure correction from Thomas et al. (2010) is also plotted (gray circles). The vertical red line and red field represent the mean temperature and standard deviation calculated using the Fe-Mn exchange between garnet-ilmenite (Grt-Ilm; Pownceby et al., 1991). The red triangles show the pressures calculated with the garnet barometer (Wu, 2019) and the blue squares represent the temperatures calculated with the garnet-cordierite (Grt-Crd) thermometer (Kaneko & Miyano, 2004). The pressure and temperature field obtained using 1wt% H_2O and the bulk rock composition in the MAGEMin package (Riel et al., 2022) for the assemblage observed in our samples is shown by the hatched triangular area. Subscripts in legend represent references: (1) Wark and Watson (2006), (2) Thomas et al. (2010), (3) Huang and Audétat (2012), (4) Pownceby et al. (1991), (5) Kaneko & Miyano (2004), (6) Wu (2019), (7) Riel et al. (2022).

From their study, Taylor and Stevens (2010) describe three stages of the "selective peritectic phase entrainment model. Peritectic garnet growth in rapid partial melts of metapelites represents the first stage of entrainment and these garnets have Mg# = 20–27, XSpss = 0.01, and

589 homogenous compositions. The second stage of entrainment is present in the peritectic garnets
590 from leucosomes, interpreted to have undergone limited recrystallization and some
591 amalgamation at high temperatures with Mg# = 20–22 and XSpss = 0.01. Finally, the garnets
592 from the granite sheets are rounded and euhedral, resulting from dissolution-precipitation
593 reactions, amalgamation, and re-equilibration with the magma. This third stage is further divided
594 into large (0.8–4 mm) garnets with Mg# = 18–21 and XSpss = 0.02 and very small (75–600 μm)
595 garnets with Mg# = 12–14 and XSpss = 0.02–0.03. Both large and small garnets from granite
596 sheets have rims with slightly lower Mg# and higher XSpss contents than their cores (Taylor &
597 Stevens, 2010). With homogenous Mg# = 12–13 and XSpss = 0.04, the garnets in our samples
598 are compositionally most similar to those from the granite sheet (Fig. 6). Additionally, the
599 presence of melt inclusions in both garnet and cordierite (Fig. 5) provides evidence for rapid
600 crystal growth (Cesare et al., 2011).

601 Taylor and Stevens (2010) also presented chondrite normalized REE data for the garnets
602 in their study. Representing the first stage of garnet entrainment, metapelite garnets have flat,
603 relatively depleted HREE patterns and weak negative Eu anomalies (Lu_N/Gd_N = 0.98–0.16,
604 Eu/Eu* = 0.5). Leucosome garnets from the second stage have slightly steeper HREE slopes and
605 much stronger negative Eu anomalies (Lu_N/Gd_N = 1.59–0.56, Eu/Eu* = 0.07). Garnets from the
606 third stage, the granite sheets, have the steepest HREE slopes and the most pronounced negative
607 Eu anomalies (Lu_N/Gd_N = 1.15–28.38, Eu/Eu* = 0.03). The strongly negative Eu anomalies of
608 the U1570 dacite garnets overlap with the latter stages of entrainment, where evidence of
609 dissolution-precipitation reactions is prominent. Taylor and Stevens (2010) also reported changes
610 in HREE slope from steeper in the core to flatter in the rim of garnet in the granite sheets, and
611 complex zonation of yttrium (Y) concentrations, which they attribute to the amalgamation of
612 grains. The HREE slopes in the Site U1570 dacite garnets cover the range presented in Taylor
613 and Stevens (2010), though most overlap with the stage three granite sheet garnets, and some
614 show evidence of the same zonation patterns from core to rim (Fig. 10). The garnets from our
615 study also have similarly complex Y zoning, with a broad pattern of Y enrichment in the cores
616 relative to the rims (Fig. 10). Finally, the bulk composition of our samples shows depletion
617 in HREE, Zr and Hf (Fig 3B, S2) consistent with the presence of residual garnet in the source.
618 Peritectic garnets are expected to be enriched in HREE (Fig. 8; Taylor and Stevens, 2010). While
619 present as large grains, the fraction of garnet in our samples is relatively small (< 2 wt.%).

Hence, if some of these newly formed grains were not entrained in the magma, they might explain the HREE (and Hf and Zr) depletion of the bulk rock.

In summary, garnet compositions in our samples have notable similarities in major and trace element compositions with peritectic phases entrained in a melt. Notably, they are chemically similar to entrained garnets resulting from dissolution-precipitation reactions grains in a magma. Through re-equilibration with the magma and amalgamation of new grains formed by peritectic reaction, dissolved metapeltic garnets can be re-precipitated with their major elements homogenized (Taylor & Stevens, 2010). These processes can produce garnets with magmatic textures, xenocrystic, homogenous, major element chemistry, and complex trace element zonation through peritectic growth in a hot, water-undersaturated magma during metapelitic melting (Clarke, 2007). At Mimir High, the main solid peritectic products which are transported within the dacite magma toward the surface are Fe-rich garnet and cordierite, resulting in a bulk rock composition with high A/CNK and Fe contents and relatively low Si and K contents (Figs. 3, 10).

5 Geothermobarometry and pseudsections

The mineral textures (subhedral morphology, melt inclusions) and mineral chemistry of the garnet and cordierite grains support their origin as products of peritectic melt reactions that have been entrained in the dacitic melt. During evolution and transport the dacite may have been impacted by variable degrees of re-crystallization and chemical re-equilibrium. As such, the observed mineral assemblage and bulk rock chemistry can be used to constrain the pressure, temperature, and water saturation conditions of melt generation of the magma.

5.1 Ti in quartz, TitaniQ thermometer

Wark and Watson (2006) formulated the TitaniQ thermometer based on the temperature-dependent substitution of titanium for silicon in the quartz matrix over a temperature range of 600–1000 °C at 10 kbar. Their equation for rutile-undersaturated rocks is:

$$T(℃) = \frac{-3765}{\log\left(\frac{X_{Ti}^{qtz}}{a_{TiO_2}}\right) - 5.69} - 273 \quad (1)$$

where X_{Ti}^{qtz} is the concentration (ppm) of Ti in quartz and a_{TiO_2} is the activity of TiO_2 in the melt.

For silicic igneous rocks that are TiO_2 undersaturated, indicated by the lack of rutile as a stable phase, the activity of titanium in the melt < 1 and must be estimated to apply TitaniQ. Ghiorso and Gualda (2013) calculated the activity of titania in the liquid relative to rutile saturation (aTiO$_2$) for the Shiveluch Volcano dacite using two independent methods: one based on the composition of coexisting spinel and ilmenite in the magma, and one calculated with rhyolite-MELTS (Gualda et al., 2012) using the rhyolitic matrix glass composition from Humphreys et al. (2008). This melt composition is comparable to the rhyolite glass in our sample with 78.0 wt% SiO_2, 7.4 wt% alkali content, 12.4 wt% Al_2O_3, and 0.3 wt% TiO_2 (Fig. 3). The two sets of calculations intersect for aTiO$_2$ between 0.75 and 0.90 for 730–800 °C (see Fig. 3 in Ghiorso & Gualda, 2013).

Using equation (1), variation of aTiO$_2$ within ± 0.1 only results in temperature variation within ± 20°C. The mean Ti concentration and its one standard deviation in quartz hosted by the dacite is 142.04 ± 37.8 ppm. Assuming aTiO$_2$ = 0.8, we obtain a mean crystallization temperature of 817 ± 42 °C (Fig. 11; Table 3).

A few studies have reformulated TitaniQ to include the effect of pressure (e.g., Thomas et al., 2010; Huang & Audétat, 2012). In their experimental study, Thomas et al. (2010) showed that the solubility of Ti in quartz decreases with increasing pressure. They present a pressure-dependent TitaniQ thermometer calibrated between 5 and 20 kbar. Huang and Audétat (2012), however, argued that Thomas et al. (2010)'s thermometer overestimates Ti solubility, and consequently the effect of pressure, in their experiments. Using new rutile-saturated experiments performed between 1 and 10 kbars, the authors proposed the following equation:

$$logTi = -0.27943\left(\frac{10^4}{T}\right) - 660.53\left(\frac{P^{0.35}}{T}\right) + 5.6459 \quad (2)$$

where Ti is the rutile-saturated concentration of Ti (in ppm) in quartz, T the temperature in Kelvin, and P pressure in kbar. For natural samples that are not saturated in rutile, $X_{Ti}^{qtz-sat}$ must be calculated using aTiO$_2$, such as $X_{Ti}^{qtz-sat} = X_{Ti}^{qtz}/a_{TiO_2}$. Temperatures calculated in our study using the Huang and Audétat (2012) thermometer and a_{TiO_2} = 0.8 range from 886 ±45 °C at 5 kbar down to 740 ±39 °C at 1 kbar (Fig. 11; Table 3).

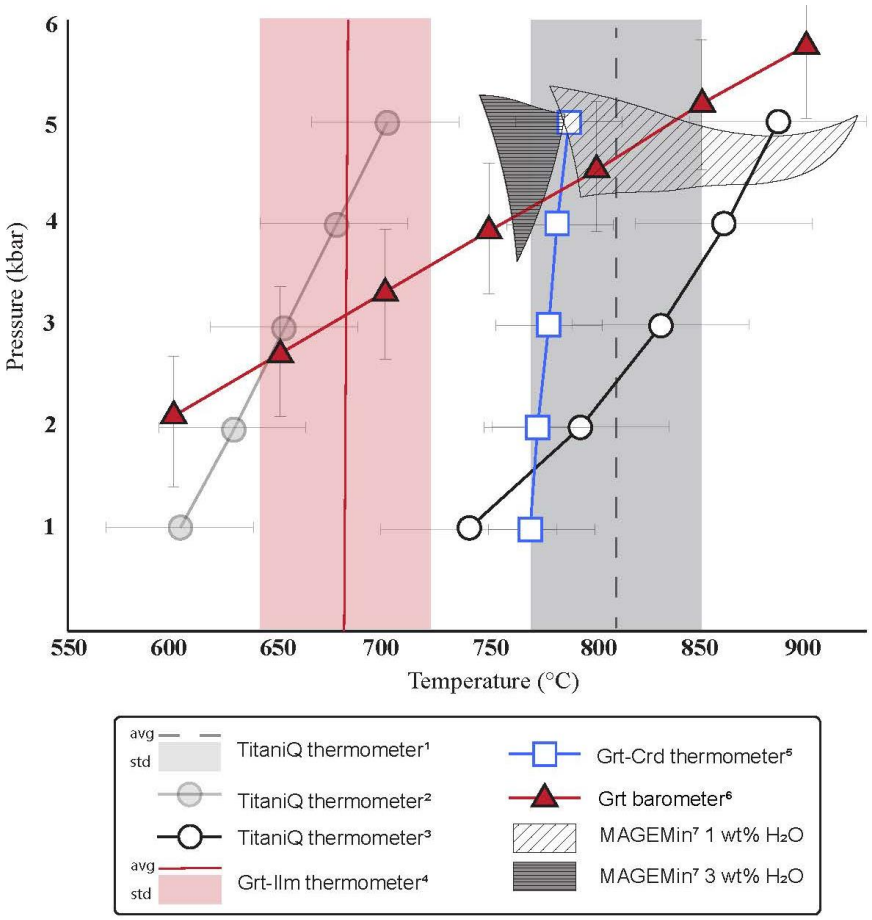

Figure 11. Schematic diagram for selective peritectic phase entrainment model for garnet grains. (1) Grains of peritectic phases from metapelitic residuum become entrained in the melt. (2) Residual grains experience limited new crystallization and amalgamate in the second stage. (3) BSE image of garnet from sample U1570A-26R2-4 representing the third stage in which amalgamated grains dissolve and re-precipitate as single grains with homogenized major element compositions but variable trace element compositions. Adapted from Taylor and Stevens (2010). LA-ICP-Ms analysis locations are represented by yellow squares; values on yellow squares are the corresponding HREE slopes (i.e., Lu_N/Gd_N, chondrite-normalized ratio). Values in black circles are the Y (ppm) concentrations at the same location. The Al_2O_3 vs. FeO wt% plot shows bulk rock compositions (yellow stars) compared to major phases including garnet (black filled

686 circles), cordierite (black open circles), plagioclase (dark gray filled circles), alkali feldspar (gray
687 open circles), quartz (light gray filled circles), and matrix glass (black open triangles).

688 **Table 3.** Summary of calculated pressure and temperature conditions of the dacite sample
689 formation estimated from thermodynamic calculations and thermobarometers on mineral phases.

		H_2O	**T (°C)**		**P (kbar)**	
MAGEMin	Riel et al., 2021	1 Wt%	725-800		1.5-3.5	
pseudosection		3 Wt%	710-720		2.9-3.2	
TitaniQ	Wark & Watson, 2006		817	± 42	1	
thermometer	Thomas et al., 2010		604	± 35	1	
$a TiO_2 = 0.8$			652	± 37	3	
			701	± 39	5	
	Huang & Audétat, 2012		740	± 39	1	
			831	± 43	3	
			886	± 45	5	
Grt-Ilm	Pownceby et al., 1991		686	± 37		
thermometer						
Grt-Crd	Kaneko & Miyano, 2004		769	± 45	1	
thermometer			778	± 45	3	
			787	± 45	5	
Grt	Wu, 2019		600		2.1	± 1.3
barometer			700		3.3	± 1.3
			800		4.6	± 1.3
			900		5.8	± 1.3

690 Pseudosection results are given as ranges for which the observed phase assemblage is stable. Thermometer
691 results are given as an average and one standard deviation or temperature with corresponding input pressures
692 if applicable. Barometers results are given as an average and one standard deviation for each input
693 temperature.

694 5.2 Garnet-ilmenite and garnet-cordierite thermometers

695 Xenocrysts present in the dacite allow for the use of the garnet-ilmenite geothermometer
696 based on Fe-Mn exchange reactions and the garnet-cordierite geothermometer based on Fe-Mg
697 exchange reactions.

698 The Fe-Mn exchange between garnet and ilmenite was investigated by Pownceby et al.
699 (1987), who developed a pressure independent geothermometer. Pownceby et al. (1991)
700 reinvestigated the original thermometer to include the influence of grossular content in garnet
701 and presented the thermometer:

$$T = \frac{14918-2200\left(2X_{Mn}^{Ilm}-1\right)+620\left(X_{Mn}^{Grt}-X_{Fe}^{Grt}\right)-972X_{Ca}^{Grt}}{R\ln K_d+4.38} - 273.15 \quad (3)$$

where R is the gas constant, T is the temperature in Celsius, X_{Mn}^{Ilm} is the molar concentration of Mn in ilmenite, and X_{Mn}^{Grt}, X_{Fe}^{Grt}, X_{Ca}^{Grt} are the molar concentrations of Mn, Fe, and Ca in garnet, respectively. K_d is the distribution coefficient defined by:

$$K_d = \frac{(X_{Mn}^{Grt})\times(X_{Fe}^{Ilm})}{(X_{Fe}^{Grt})\times(X_{Mn}^{Ilm})} \quad (4)$$

Using experimental results performed at 600–1000 °C and 10 kbar and $FeTiO_3$-$MnTiO_3$ activity data, their thermometer has a resolution of ± 30–50°C. In our study we only used this thermometer on ilmenite inclusions in garnet to account for the rapid diffusion of Fe-Mn in ilmenite. In fact, the relatively slow Fe-Mn diffusion in garnet effectively shields the ilmenite from re-equilibration and records temperatures for garnet growth (Pownceby et al., 1991). Garnet-ilmenite temperature results for seven garnets in the dacite give an mean of 686 ± 37 °C (Fig. 11; Table 3).

The garnet-cordierite geothermometer is commonly used to determine temperatures in high-grade amphibole and granulite facies metamorphic rocks (Spear & Selverstone, 1983). However, it is considered to be a poorly calibrated thermometer because cordierite is prone to severe alteration in high-grade metapelites. We note, however, alteration is not observed in our sample (Figs. 4, 5). In addition, the presence of a garnet inclusion in cordierite (Fig. 5C) supports chemical equilibrium between the two phases. Several calibrations have been proposed for this thermometer (e.g., Thompson, 1976; Holdaway & Lee, 1977; Perchuck et al., 1985; Wells, 1979). Here we present results obtained with Kaneko and Miyano (2004)'s calibration:

$$T = \frac{-26144.7+\left(-0.122+W_V^{Grt}\right)(P-1)+W_H^{Grt}-80.44(Mg^{Crd}-Fe^{Crd})}{-12.7094-R\ln K_d+W_S^{Grt}+1.642(Mg^{Crd}-Fe^{Crd})} - 273.15 \quad (5)$$

where T is Celsius, and P is in bar. The W_H^{Grt}, W_S^{Grt}, and W_V^{Grt} are the non-ideal mixing terms for the garnet solid solution based on Berman (1990)'s expression (see equations A5, A6, and A7, respectively in Kaneko and Miyano, 2004). The terms Fe^{grt}, Mg^{cd}, etc. denote the molar fractions of Fe and Mg in the garnet and cordierite solid solutions such as Mg^{Crd} = Mg/[Mg + Fe] , and Mg^{Grt} = Mg/[Mg + Fe + Ca + Mn], with Mg, Fe, Ca and Mn in mol. %. Finally, the exchange coefficient (K_d) defined by:

729 $$K_d = (Fe^{Grt})/(Mg^{Grt}) \times (Mg^{Crd})/(Fe^{Crd}) \quad (6)$$

730 The estimated absolute error for Kaneko and Miyano (2004)'s calibration is ± 45°C.
731 Calculated temperatures using the compositions of garnet and cordierite grains in our samples
732 and equation (5) and (6) show significantly higher temperatures (~770-790 °C, Fig. 11; Table 3)
733 than the garnet-ilmenite thermometer, with an effect of pressure smaller than the estimated
734 uncertainty on the temperature.

735 5.3 Garnet barometer

736 While commonly used to determine pressures for metapelites, the garnet-Al_2SiO_5-
737 plagiocalse-quartz (GASP) barometer (Holdaway, 2001) cannot be applied to our samples due to
738 the absence of an aluminosilicate and biotite in the assemblage. Additionally, the garnet-rutile-
739 ilmenite-plagioclase-silica (GRIPS) barometer (Bohlen & Liotta, 1986) is not recommended for
740 pressures below 6 kbar (Wu & Zhao, 2006). Instead, we use the garnet barometer developed by
741 Wu (2019) for metapelitic assemblages to estimate the pressure recorded by the phase
742 assemblage in our samples. In fact, Wu (2019)'s barometer was initially developed because
743 plagioclase is often CaO-poor or absent in metapelites, making barometers such as GASP and
744 GRIPS less precise or unusable. It is empirically calibrated using natural metapelite samples with
745 pressure and temperature conditions of 1–15 kbar and 430–900 °C for garnets with molar
746 fractions of calcium and iron in the solid solution of 0.02–0.29 and 0.42–0.91, respectively:

747 $$P\ (bar) = \frac{-8904.5+24.542T\ +0.45RT\ln(Ca^{Grt}/Fe^{Grt})+0.15aT+0.15c}{1-0.15b} \quad (7)$$

748 T is in Kelvin and a, b, and c are polynomial coefficients (see equations (5), (6), and (7),
749 respectively in Wu (2019), which account for differences of excess chemical potential between
750 grossular and almandine components in the garnet solid solution; Holdaway, 2001). The
751 estimated error for pressures calculated using equation (7) is less than ±1.3 kbar. Using our
752 sample's mean garnet composition (Table 2), we obtain a range of pressures from ~2.1 kbar at
753 600 °C to ~5.7 kbar at 900 °C (Fig. 11; Table 3).

754 5.4 Pseudosections

755 The phase assemblage calculated with MAGEMin (Riel et al., 2022) that includes garnet
756 (grt), cordierite (crd), ilmenite (ilm), two feldspars (fsp^2), quartz, (qz), spinel (spl), and silicate

melt (m) best matches the assemblage observed in the Site U1570 dacite. The pseudosection calculated with 1 wt% H_2O shows this assemblage being stable at 775–915 °C for pressures between 4.3–5.3 kbar (Fig. 12; Table 3). With 3 wt% H_2O, the range of temperatures over which the phase assemblage observed in our samples is stable is much narrower (750 °C and 790 °C) but the pressure range is expanded (3.7–5.2 kbar; Fig. S8; Table 3).

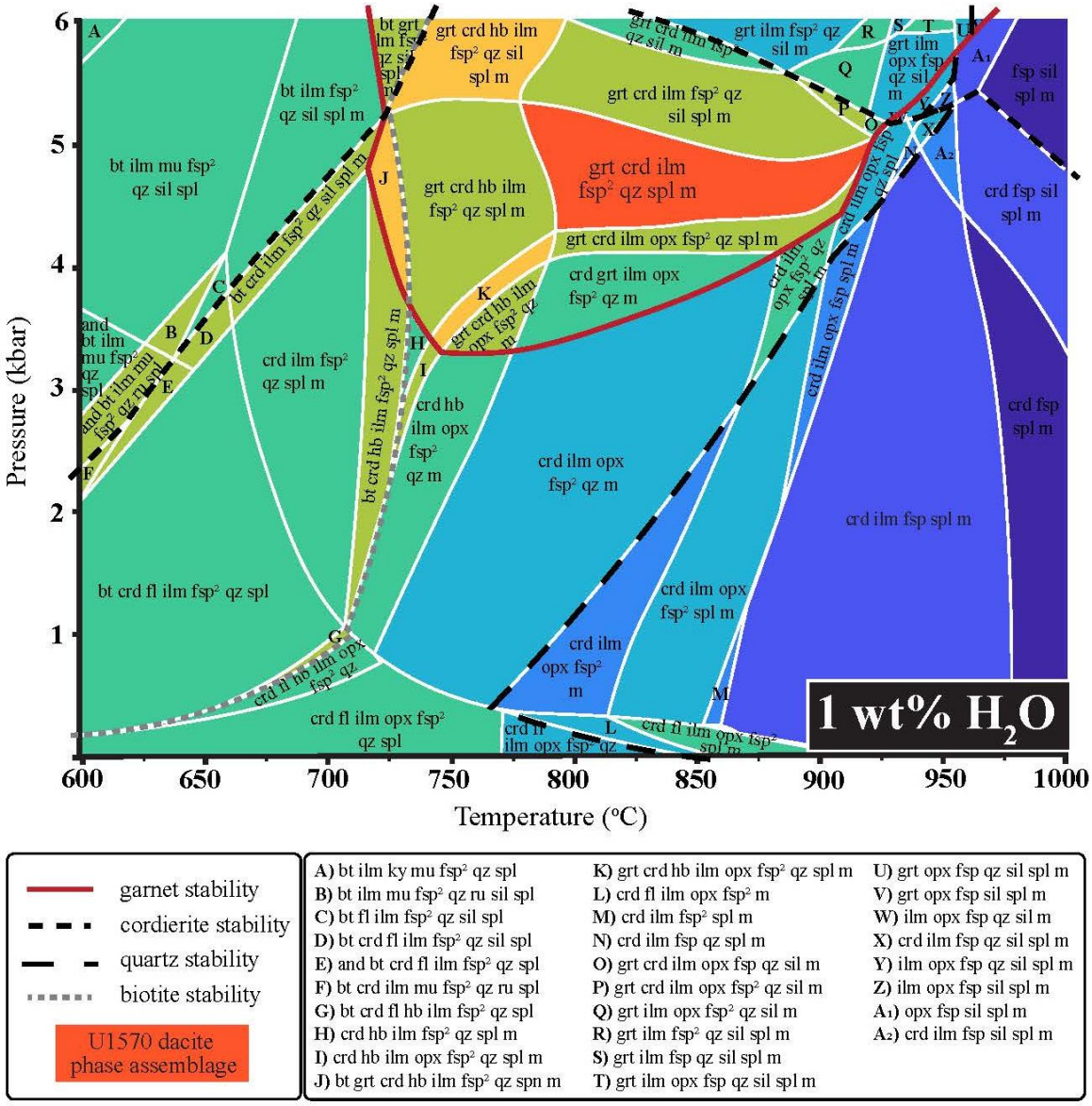

Figure 12. Pseudosection calculated from the bulk rock composition acquired on the sample U1570-26R2-51-54 (Fig. 2D), assuming 1 wt % H_2O contents, using the MAGEMin thermodynamic package (Riel et al., 2022). Colored fields ranging from blue to yellow represent an increasing number of phases in an assemblage; the dark orange field represents the one that reproduces the phase assemblage observed in the U1570 dacite (grt-crd-ilm-fsp^2-qz-spl-m).

768 Garnet stability field is represented by the solid red line, cordierite stability field with a black,
769 short-dashed line, quartz stability field with a black, long-dashed line, and biotite stability field
770 with a gray, dashed line. Phases include: andalusite (and), biotite (bt), cordierite (crd), ternary
771 feldspar (fsp, fsp^2 indicates two compositions of ternary feldspar), garnet (grt), hornblende (hbl),
772 ilmenite (ilm), muscovite (ms), olivine (ol), quartz (qz), sillimanite (sil), spinel (spl, spl^2
773 indicates two compositions of spinel), silicate melt (m), and aqueous fluid (H_2O). Calculations
774 with 3 and 5wt% H2O in the bulk compositions are shown in Fig. S8.

775 Finally, this phase assemblage is not reproduced in the pseudosection calculated with 5 wt%
776 H_2O. The pressure and temperature range where garnet, cordierite, and quartz overlap (~3.3 kbar,
777 ~675–700 °C) also includes amphibole in the assemblage and lacks the two feldspars (Fig. S8;
778 Table 3). In the following, we therefore assume that the bulk water content of the Site U1570
779 dacite is low (< 3 wt% H_2O).

780 **6 Discussion**

781 6.1 Dacite origin and emplacement

782 To understand the potential implications that dacite from Site U1570 may have for large
783 igneous province emplacement, continental breakup, and thermogenic gas production, it is
784 necessary to consider its petrogenesis. Below we discuss (1) the emplacement of the dacite using
785 textural observations and stratigraphic constraints and (2) the origin of the dacite with results
786 from thermodynamic calculations, thermobarometry, and phase composition analyses.

787 *6.1.1 Stratigraphic constraints*

788 The highly vesicular nature of the unit is consistent with emplacement of the dacite in a
789 shallow environment at low pressure (Fig. 4, 5). For evolved melts, highly vesicular pyroclasts
790 (>80% vesicularity) only form above water depths of 500 m, unless the dissolved magmatic
791 water content is unrealistically high (>7 wt%; Wright et al., 2003). Dacitic melts containing a
792 few wt% water may be expected to have viscosities of 10^7 to 10^6 Pa.s for pure melt between 750
793 and 850 °C (Giordano et al., 2008). Such melts would be prone to explosive fragmentation
794 during transport to the surface, with exsolution of the volatiles and formation of vesicles
795 resulting in increasing bulk viscosity and further promoting fragmentation. Such rapid
796 decompression and explosive fragmentation is also supported by the fragmentation of the large

mineral grains observed in the samples (Figs. 4,5; e.g., Best & Christiansen, 1997; Bindeman, 2015).

In order to assess the emplacement conditions of the dacite unit, several temperature and chemical proxies were measured from the surrounding sediments. The total organic matter (TOC) record shows no systematic loss of TOC in the sediments surrounding the dacitic unit. Moreover, no significant variations in $\delta^{13}C_{org}$ (Fig. 2) occur near the dacite unit and no appreciable organic-matter maturation appears to have taken place near the dacite based on the RockEval parameters (Tmax), which would be expected even at relatively low temperature (<100 °C; Svensen et al., 2023; Bédard et al., 2023). Analyses performed on sediment samples from directly overtop the dacite in borehole U1570D show high Hg concentrations (~350 ppb), however, these concentrations remain within the variability of the rest of the analyzed samples. Svensen et al. (2023) demonstrated that thermal alteration in intrusive aureoles can result in a loss of sedimentary Hg, likely because the most common sedimentary Hg phases (organic-matter bound Hg and HgS) rapidly volatilize at temperatures of 200–300 ºC, therefore, elevated Hg is not consistent with thermal impacts from the dacite (e.g., Biester & Scholz, 1997).

Finally, samples were collected from directly at and within the mixing zone at the top and base of the unit, as well as in a transect away from the contact and prepared for palynological analyses. Samples in the mixing zone and adjacent to the dacite yielded abundant thermally immature assemblages of acritarchs, dinocysts, pollen, and spores. These assemblages yielded a Thermal Alteration Index (TAI; Gutjahr, 1966; Staplin, 1969) of 1+, values that were also recorded from similar palynofloras 20 m further down the core. These TAI values are indicative of temperatures of <45°C and confirm that the dacite did not thermally alter the sediments into which it was recovered. This combined evidence from the sediments, along with the pyroclastic nature of the unit, strongly argues against emplacement of the dacite as a liquid magmatic intrusion. Although, emplacement as an invasive lava flow could explain the mingling textures evident on the upper margin (Famelli et al., 2021), it is also inconsistent with the pyroclastic nature of the dacite. The alternative, and preferred, interpretation is that the unit comprises a deposit associated with an explosive pyroclastic density current (PDC; Branney et al., 2021). Explosive pyroclastic density currents are known to be capable of flowing subaqueously if their density exceeds that of the water in which they are erupted (Sparks et al., 1980a, b; White, 2000). The flow of PDC's below water is in large part density-controlled, and, as such, the potential for

a PDC to flow into other fluids, such as muddy unconsolidated basin floor sediments, should be equally controlled by density and other rheological properties, such as shear strength and cohesion of water saturated sediments which will restrict the depth to which a PDC could become invasive (e.g., Owen, 1987). The relatively sharp contact between the base of the dacite and sediment below (Fig. 2E) with preserved sediment structures and local incorporation of sediment clasts indicates some level of basal erosion and incorporation during the emplacement of the dacite as a PDC (e.g., Roche et al., 2013). The emplacement dynamics of the dacite clearly merit further study, however, we tentatively propose emplacement as a subaqueous PDC, which exceeds the density of the uppermost layer of unconsolidated, mud-rich basin sediments, promoting it to be partially invasive and resulting in local mingling with sediments.

6.1.2 Thermobarmetric and H_2O constraints

Ideally, we would construct the pseudosections and perform thermobarometric calculations using the composition of the protolith (e.g., Álvarez-Valero and Waters, 2010) from which the dacite was derived to estimate the pressure and temperature conditions and water contents of formation. In our case, however, we do not have access to the composition of the protolith. Because the textural and chemical characteristics of garnet, cordierite and alkali feldspar that these minerals are peritectic phases (see equation 9), they should be in equilibrium with the melt. The anorthite (An) contents of the plagioclase are more variable (Fig. S5a). We compare plagioclase found in our samples with plagioclase grains found in lavas from El Hoyazo, Spain (Hiwatashi et al., 2021). The occurrence of high K-volcanics in this province can be considered as an analog for the formation of the dacitic unit studied here (see below). Plagioclases in the lavas from El Hoyazo show a large compositional spread with An-rich plagioclase (>80%) showing resorbed or patchy textures, intermediate compositions showing oscillatory zoning, and An-poor (<50%) compositions occurring in homogeneous subhedral grains. Hiwatashi et al. (2021) interpret this variability as evidence for magma mixing between high-SiO2 dacite and andesite. Plagioclase observed in our samples overlap with the compositions of the homogeneous grain interpreted as in equilibrium with a dacitic magma. Hence, using the bulk rock composition, we consider that the pressure-temperature field that reproduces the phase assemblage observed in our sample provides a good approximation for the conditions of formation of the magma.

Partial melting of metapelitic rock during metamorphism commonly produces almandine garnet, which has commonly been interpreted as a high-pressure (>7 kbar) peritectic or liquidus phase in a hydrous, Al-rich magma (Green & Ringwood, 1968; Clemens & Wall, 1988; Harangi et al., 2001; Sieck et al., 2019). Green (1977), however, demonstrated that the grossular and spessartine content of almandine garnets are sensitive to pressure and that Ca and Mn-rich (> 4 wt% CaO and MnO) almandine garnets could have crystallized at pressures less than 5 kbar. However, this cannot explain low-pressure signature recorded by the almandine garnet in our samples as they are Ca-poor (~1 wt% CaO) and Mn-poor (~1.8 wt% MnO). Aranovich and Podlesskii (1983) experimentally investigated the cordierite-garnet-sillimanite-quartz equilibrium at 4–8 kbar to determine the coexisting garnet and cordierite equilibrium compositions. At 4 kbar and 700°C, their experimental products have Fe-rich compositions consistent with natural samples from their study. They also showed that the Mg content of garnet and cordierite increases significantly with pressure from Mg^{grt} = 0.10 mol% and Mg^{crd} = 0.44 mol% at 4 kbar to Mg^{grt} = 0.51 mol% and Mg^{crd} = 0.89 mol% at 8 kbar. Compared to the Mg content measured in garnet and cordierite grains in our study (Mg^{grt} = 0.10 ± 0.1 mol% and Mg^{crd} = 0.41 ± 0.02 mol%), their results support the relatively low equilibration pressure calculated for our samples. Additionally, Clemens and Wall (1981) observed garnet crystallization down to 1 kbar for temperatures 700–900 °C in their experiments for water-undersaturated, peraluminous magmas, and in the last decade, several studies, through thermodynamic calculations and characterization of melt inclusions (e.g., Acosta-Vigil et al., 2010; Bartoli et al., 2013a, 2013b), have shown that peritectic garnet can also grow at low temperatures (≤ 700°C) and low pressures (≤ 5 kbar).

Growth of peritectic garnet, cordierite, and alkali feldspar during anatexis of metapelites is thought to result from the breakdown of biotite during dehydration melting (e.g., Cesare et al., 2009; Ferrero et al., 2012; Stevens et al., 2007). Weinburg and Hasalová (2015) cite the following reaction in metapelites and variable pressure and intermediate temperature (700–800°C; Le Breton & Thompson, 1988; Spear, 1993):

Biotite + Quartz + Plagioclase + Aluminosilicate = Garnet/Cordierite + Alkali Feldspar + melt (8)

in which cordierite results from the subsequent breakdown of garnet (Stevens et al., 1995). The absence of biotite in our sample, the dissolution texture observed on the margins of plagioclase grains, and the existence of a garnet inclusion in cordierite support the proposed reaction for peritectic garnet growth (Eq. 8). Our results are consistent with biotite dehydration melting, because its absence in our samples suggests that the magma formed at temperatures higher than the field of stability of biotite (<350 °C for <3 wt% H_2O).

The phase assemblage observed in our samples is only reproduced for bulk water contents ≤ 3wt%. A water-undersaturated composition is additionally supported by the presence of graphite in the assemblage and anhydrous cordierite grains suggested by high analytical totals (Table 1). In fact, for any H_2O-bearing phase, such as melt or cordierite, to coexist with graphite, it must have an $a_{H2O} < 1$ (Bartoli et al., 2013c). Although metapelitic anatexis at high temperature (700–800°C) is facilitated by biotite dehydration melting and the release of water, experimental studies by Holtz et al. (1992) show that the melt remains water-undersaturated. Additionally, these water-fluxed, undersaturated melts are particularly buoyant, supporting rapid migration to the surface (Holtz et al., 1992).

Using the pseudosection results for a magma with 1–3 wt% H_2O, the observed phenocryst assemblage for our samples is stable at pressures of ~4–5 kbar and temperatures higher than 750 °C, consistent with results obtained from thermobarometric calculations (Fig. 11). The pressures and temperatures recorded by the dacite phase assemblage are considered to approximate the conditions of the last equilibrium state of the magma prior to rapid transport and quenching. The limited compositional variability of the glass and mineral phases, as well as the highly vesicular and glassy texture of the matrix, are interpreted to be consistent with rapid emplacement and quenching. Therefore, we highlight that the recorded pressure-temperature conditions may not represent the original melting conditions and the sample may have re-equilibrated at depth along its ascent path (e.g., Álvarez-Valero & Waters, 2010).

We note that while crystallization and heat loss from the breakdown of garnet during the decompression of magma should result in a lower temperature for Grt-Crd pairs than for Grt-Ilm pairs (Sykes & Holloway, 1987), our samples record significantly higher temperatures for the Grt-Crd pairs (Fig. 11). Hence, these results are consistent with a progressive melting process happening at a relatively constant low pressure and variable high temperatures, with garnet-

ilmenite pairs recording the early stage of melting and garnet-cordierite pair the final stage of melting. Therefore, we consider ~4.5 kbar, ~800 °C, and 1–3 wt% H_2O to be a good approximation of the conditions for the average peak temperature during the formation of the dacitic magma. Because seismic profiles of the Mimir High show the sediment cover is relatively thin where the dacite was collected (Fig. 2), we can assume this pressure range is more likely to result from generation at depth within the crust rather than from intrusion into the sediments (Abdelmalak et al. 2017; Polteau et al., 2020).

6.1.3 Age constraints

McKenzie et al. (2018) suggest that the REE abundances in zircon preserve a record of the composition of silica-rich parental melts since REE diffusion in zircon is slow and Zr is abundant and incompatible in silica-rich melts. This means that variation in REE patterns, like Eu anomalies, are representative of different parental magmas. Compared to population #1, population #2 zircons show significantly more variable Eu anomalies (Fig. S9), indicating they come from different sources and are therefore inherited rather than crystallized directly from the dacite. The higher variability of population #2 is also observed on the shape components of the trends (i.e., lambda coefficients; Anenburg & Williams, 2022), even when the Ce and Eu anomalies are not included (Fig. S9C). The more restricted range of concentrations observed in population #1 is consistent with crystallization from a single melt phase, likely during peritectic growth of garnet and cordierite. The spatial distribution of these populations on CL images of the individual zircons indicates that population #1 analyses are more often located on the rims of grains, while population #2 analyses are either in or on the edge of darker cores (Fig. 9A). This suggests that the population #1 analyses likely represent new growth from the dacite magma reaching zircon saturation and that the calculated weighted average of these analyses (54.6 ±1.1 Ma) is interpreted as the magmatic age. We note that as the analyzed zircons were found as inclusions in garnet and cordierite, this age corresponds to the maximal age (not storage at depth) for the eruption age.

The kernel density estimate (KDE) plot of the spot ages from population #2 shows zircon as old as 2500 and 1700 Ma, with additional peaks at 100–400 Ma (Fig. S7A). This is in range of what is expected for inherited grains on the Vøring Plateau, with possible contributions from East Greenland sources (450–350 Ma, 2000–1700 Ma, and 3800–2500 Ma) and Norwegian

sources (450–350 Ma, 1250–900 Ma, and 1750–1500 Ma; Fonneland et al., 2004). However, it should be noted that our calculations only include 11 analyses for population #2 and are therefore unlikely to be a statistical representation of the entire spectrum of inheritance ages.

Zircons tend to incorporate HREEs relative to LREE and middle REEs (MREEs) from their host melt (McKenzie et al., 2018). Chondrite-normalized (McDonough & Sun, 1995) REE spectra for zircon measured in our samples are broadly consistent with this magmatic zircon trend with steep positive slopes (Fig. S9A). There are a couple of analyses that have elevated LREE concentrations. Because REE diffusion in zircon is slow, this may be the result of overlapping inclusions during analysis or can be an effect of hydrothermal alteration as an influx of LREE (Hoskin, 2005; McKenzie et al., 2018). The trace element concentrations for these analyses do not suggest analytical overlap with other minerals and both are in older population #2 grains. Therefore, we suggest their LREE concentration results from hydrothermal alteration, and neither of these zircon grains are used in further interpretations.

6.2 Regional implications

6.2.1 The evolution of rifting on the Vøring Plateau

Crustal anatexis at magma-rich margins during rifting is often considered to be a lower crustal process, facilitated by a mafic magmatic underplate. Crustal magmas are then transported to an upper crustal reservoir or to the surface with varying degrees of re-equilibration and crustal assimilation during transport (e.g., Vissers et al., 1995; Pederson et al., 1998 and references therein; Platt et al., 1998; Duggen et al. 2004; Álvarez-Valero & Kriegsman, 2007; Thybo & Artemieva, 2013 and references therein; Neumann et al., 2013). Dacite generation through underplating has been described by Luo et al. (2018) as a result of crustal anatexis from heat provided by mantle-derived basaltic magmas. The basaltic magmas mix with the crustal melts to produce andesitic magmas, which can evolve to strongly peraluminous dacitic magmas by stalling, fractionating, and the assimilation of anatectic melts of surrounding metasedimentary rocks. The presence of underplated material at the base of the crust is often supported by seismic reflection images of thick, lower crustal bodies with high velocities (V_P > 7 km) that are characteristic of magma-rich margins (Kelemen and Hobrook; 1995; White et al., 1987, 2008; Gac et al., 2022). In the Jameson Land Basin in East Greenland and in the Artic Basin of North

Greenland, the underplated material has also been proposed as a source of melt generation (Thorarinsson et al., 2011; Eide et al., 2022).

Our thermobarometric calculations suggest, however, that the dacite collected at site U1570 was not produced in the lower crust but was instead generated in the upper crust (< 18 km depth assuming a continental crust density of 2.8 g/cm^3). The bulk trace elements composition of the samples (Fig. 3B) also supports an upper crust origin. The enrichment in Cs, in particular, has been proposed as a discriminating factor between the upper and the lower crust (Meyers et al., 2009). No evidence of deeper crustal processes is observed. This may be explained by chemical re-equilibration in an upper crustal reservoir of a magma formed at depth. For instance, this scenario has been favored to explain the formation of the high-K volcanic lavas in the NVP, SE Spain. Thermobarometric calculations performed on enclaves of the high-K volcanic rocks from the El Hoyazo and Mazarrón volcanoes suggest melting pressures of 7 kbar (Cesare et al., 1997; Cesare & Gómez-Pugnaire, 2001) and 4 kbar (Cesare et al., 2003), respectively. The difference in pressure recorded at the two volcanoes is attributed to varying depths of magma stagnation in the crust. The dacite from our study presents mineral phase compositions that match the mineral phases of the NVP high-K volcanic rocks (Figs. 6, 7, 8) and records pressure and temperature conditions of anatexis similar to those reported for the Mazarrón volcano, consistent with an upper crustal origin. Additionally, in comparison to the NVP, the glass composition (Fig. 3) in the Site U1570 dacite is more homogenous, which suggests that magma storage for our samples was long enough to approach chemical equilibrium. However, temperature recorded by the garnet-ilmenite and the garnet-cordierite pairs suggest they formed as a result of heating at a constant pressure rather than through decompression processes as we would expect for migration from the lower to upper crust. We propose the Site U1570 dacite is the product of low pressure (<5 kbar) partial melting of crustal metapelites on a thinned lithosphere, consistent with previous assumptions on the origin of silicic magmatism in the NE Atlantic (e.g., Abdelmalak et al., 2016; Eldhom et al., 1987; Sinton et al., 1998; Viereck et al., 1988) as the result of crustal anatexis at low pressure. This scenario is also consistent with a study of the Isle of Rum, in which rhyodacites were interpreted to be produced by melting amphibolite rather than deep crustal granulite (Meyer et al., 2009b), and with ODP Site 642E dacite trace element data that are compatible with melting Caledonian metasedimentary rocks (Viereck et al., 1988). Our results also provide evidence for

Previously published Ar-Ar dating on plagioclase from the dacite collected by ODP in hole 642E did not provide a precise age of eruption of the silicic magmatism (57–51.5 Ma; Sinton et al., 1998). It is, however, consistent with the age obtained on dacitic lava recovered from the North Rockall Trough (Darwin Complex; Fig. 3; Morton et al., 1988a) indicating an age ~55 Ma (Sinton et al., 1998 and references therein) and both are coincident with the magmatic age reported in this study. Importantly, the weighted mean U-Pb date interpreted as the age of zircon growth in this study (54.6 ± 1.1 Ma) postdate the age of the PETM (56–55.8 Ma; Jones et al., 2023).

Dacite recovered at ODP Site 642E is thought to have been emplaced before the peak of magmatism (Abdelmalak et al., 2017), and stratigraphic relationships indicate that the basalt overlying the silicic lavas from the North Rockall Trough and the Vøring Plateau erupted shortly after the silicic magmas (Sinton et al., 1998 and references therein). This resulted in interpretations suggesting the end of silicic magmatism is coeval with the onset of the main basaltic phase, potentially due to a change of extension rate (e.g. Abdelmalak et al., 2016; Sinton et al., 1998). Interestingly, the dacite recovered at Site U1570 is not overlain by basaltic magmatism but was rather emplaced at the surface in a shallow marine setting. At Mimir High, the overall palynofacies of the sediments is dominated by terrestrial elements (pollen, spores, and phytodebris) in addition to marine elements (dinoflagellate cysts), suggesting that the depositional environment was coastal for most of the Paleocene and Eocene (Planke et al., 2023). This demonstrates that the coastal environment was sustained despite being an active depocenter, consistent with substantial subsidence of the continental crust during extension. The emplacement of the dacite within these sediments indicates this extension remained active during and after the emplacement of this dacite.

Several studies (e.g., Peron-Pinvidic et al., 2013, Tugend et al., 2018; Gillard et al., 2019; Ferrand, 2020) have proposed that magma-rich rift margins may go through a period of hyperextension, suggesting that extreme crustal thinning does not preclude the emplacement of a high volume of magmatism. Tugend et al. (2018) suggested that when the distinction between magma-poor and magma-rich margins reflect the magmatic productivity, the overall evolution before breakup may only reflect the timing of decompression melting relative to thinning of the margin. In this context, Ferrand (2020) proposed that the Vøring margin was initiated as a magma-poor margin and was subsequently affected by hotspot-induced magmatic processes and

overprinted by volcanic activity. Evidence for silicic magmatism in the Northeast Atlantis as old as ~62 My ago, with tuff interlayers between basalt flows on the Isle of Muck (Emeleus et al., 1996) dated at 62.8–62.4 Ma (Pearson et al., 1996) and ash layers in sediments of the North Sea (Knox & Morton, 1998; Morton et al., 1998 that indicate mixing between silicic and basaltic magmatism dated at 62–60 Ma. Together, these ages suggest a longer period of crustal anatexis off the coast of Norway during rifting of the Northeast Atlantic. Additionally, the occurrence of dacitic magmatism on the mid-Norwegian margin, either overlain by subaerial magmatism (ODP hole 642E and the North Rockall Trough) or emplaced in a sediment of an early Eocene age (IODP Expedition 396, Site U1570), indicates that magmatism not only occurred at the zone of plate separation, but also landward of the ocean-continent transition on the European side. We propose that the pre-breakup phase during the development of the Vøring margin was associated with significant continental lithospheric extension. This extension resulted in low-pressure melting of metasedimentary rock to generate silicic magmas that erupted later.

6.1.2 Implications for the Paleocene-Eocene carbon cycle pertrubations

Excess magmatism, thermogenic gas release and sediment melting from contact metamorphism around sills have been invoked to explain the carbon cycle perturbations that occur throughout the late Paleocene and early Eocene, most notably the PETM, the largest of a series of global warming episodes (e.g., Svenson et al., 2004; Westerhold et al., 2020). The PETM was marked by rapid surface warming (~5 °C), ocean acidification, and the release of ^{13}C-depleted carbon into the oceans and atmosphere, evidenced by a sharp decrease in sedimentary $\delta^{13}C$, a negative Carbon Isotope Excursion (CIE; Kennet & Scott, 1991; Zeebe et al., 2009). Estimations provided by mass balance calculations suggest the PETM CIE was the result of the injection of 3,000–14,900 gigatons (Gt) of ^{13}C-depleted carbon (Zeebe et al., 2009; Gutjahr et al., 2017; Haynes and Hönisch 2020) most likely over a geologically rapid (few thousand years) time frame (Zeebe et al., 2016; Kirtland-Turner & Ridgewell, 2016). While sedimentary proxy and stratigraphic evidence support a contribution from volcanic outgassing (e.g., Frieling et al., 2016; Jones et al., 2019; Kender et al., 2021), it remains unclear whether the volcanic source would provide the timing, composition, magnitude, and rate of outgassing required to generate the CIE (Haynes & Hönisch, 2020; Gutjahr et al., 2017). It has been proposed that mafic intrusions related to the excess magmatism of the mid-Norwegian margin

resulted in hydrothermal vent complex formation and direct emission of CO_2 into the atmosphere (e.g., Gernon et al., 2022) or contact metamorphism of organic-rich ocean sediments and subsequent explosive release of large amounts of methane with a ^{13}C-depleted isotope signature ($\delta^{13}C$; e.g., Svensen et al., 2004; Frieling et al., 2016). Rampino (2013) further suggested that the NAIP emplacement may have contributed more thermogenic gases by anatectic melting of organic-rich sediments rather than pure contact metamorphism. The authors proposed that dacitic flows observed throughout the Norwegian continental margin may be the direct product of this process. Our dacitic sample from the Mimir High does not support Rampino (2013)'s hypothesis. In fact, the sediments in contact with the dacite indicate no thermal alteration, which suggests that its emplacement did not mobilize or volatilize significant amounts of carbon from surrounding sediments. While the graphite film observed on some grains suggests that minor amounts of fluid-deposited carbon may be present (e.g., Luque et al., 1993), the presence of graphite grains (as inclusion or disseminated in the sample) is consistent with a restitic phase that has been entrained in the melt (Zeck 1970, 1992). Hence, the presence of graphite is likely inherent to the nature of protolith of our samples, a graphitic metapelite, rather than a product of melting or burning organic matter.

However, this does not imply the formation of the Site U1570 dacite did not release CO_2. Cesare et al. (2005) showed that in relatively reducing conditions (as in graphitic metapelites), biotite is the only source of Fe^{3+}, with the melting reaction of biotite is important to iron reduction. As the melt produced during the reaction is relatively iron-poor (Table 1), biotite breakdown is accompanied by carbon oxidation and the production of CO_2. The amount of CO_2 produced in this way, however, is likely too small to be a significant contribution to the PETM. Additionally, the zircon inclusions record post-PETM U-Pb magmatic ages. Sill intrusions and hydrothermal vent complexes can release large volatile concentrations into the atmosphere and may have contributed to the onset and longevity of the PETM (Frieling et al., 2016; Berndt et al. 2023), but the dacite sample outlined by this study is not an example of this. In fact, the long period of silicic magmatism (~62–54.6 Ma) in the Northeast Atlantic highlighted here warrants caution in including NAIP-related thermogenic carbon released from eruptions into wet sediments in carbon emission calculations.

5 Conclusions

The garnet and cordierite-bearing dacite sampled during IODP Expedition 396 in boreholes U1570A and U1570D was likely emplaced as a high-density pyroclastic current into wet, unconsolidated sediments in a shallow coastal environment after the onset of the PETM. This is evidenced by the folded, elongated glassy pyroclastic textures, local mingling with sediment and preserved sediment clasts, and highly fragmented phenocrysts. The chemical signatures of the peritectic garnet and cordierite grains suggest an upper crustal, metapelitic protolith. This is further supported by the inheritance patterns observed in the zircon U-Pb ages that match inherited grains on the Vøring Plateau. Our thermodynamic results suggest the magma is water undersaturated ($\leq$ 3 wt% H_2O) and indicate low pressure (<5 kbar), high temperature (~800 °C) anatexis in the upper continental crust.

We propose this dacite is a crustal anatectic product of an intense and long (> 7 Myr) phase of continental stretching that preceded the main phase of basaltic magmatism emplacement, that was later (< 54.6 ±1.1 Ma) emplaced on top of unconsolidated wet sediments. Implications of lithospheric thinning in excess-magmatic margins should be considered in tectonic reconstructions for the evolution of the North Atlantic rift margin.

Data Availability Statement: All the data are shared in tables in the main text and as supplementary tables attached with this manuscript and will be archived on Zenodo upon acceptance.

Acknowledgments

We would like to thank all crew, drilling team members and lab technicians onboard the R/V JOIDES resolution. The onshore science party also included Joyeeta Bhattacharya, Reina Nakaoka, and Mengyuan Wang. For assistance with analytical techniques, we thank Clay Jones (SEM), Wil Mace (EPMA), Diego Fernandez, Christopher Anderson, and Brad Munk (LA-ICPMS), and Andrew Kylander-Clark (LASS). This study benefited from discussions with J. Bartley, J.C. de Obseo, and M.M. Abdelmalak. This work was supported by the U.S. Science Support Program, IODP, and the donors of ACS Petroleum Research Fund under Doctoral New

Investigator Grant 61305-DNI8. S.L. served as Principal Investigator on ACS PRF 61305-DNI8 that provided support for A.M. S.L. also acknowledges funding from NSF grant EAR-1946346. J.F. acknowledges funding from UK IODP grant NE/W007142/1.

References

Abdelmalak, M. M., Meyer, R., Planke, S., Faleide, J. I., Gernigon, L., Frieling, J., Sluijs, A., Reichart, G. J., Zastrozhnov, D., Theissen-Krah, S., Said, A., & Myklebust, R. (2016). Pre-breakup magmatism on the Vøring Margin: Insight from new sub-basalt imaging and results from Ocean Drilling Program Hole 642E. *Tectonophysics*, *675*, 258–274. doi.org/10.1016/j.tecto.2016.02.037

Abdelmalak, M. M., Faleide, J. I., Planke, S., Gernigon, L., Zastrozhnov, D., Shephard, G. E., & Myklebust, R. (2017). The T-Reflection and the deep crustal structure of the Vøring Margin, offshore mid-Norway. *Tectonics*, *36*(11), 2497–2523. doi.org/10.1002/2017TC004617

Acosta-Vigil, A., Buick, I., Hermann, J., Cesare, B., Rubatto, D., London, D., & Morgan VI, G. B. (2010). Mechanisms of crustal anatexis: A geochemical study of partially melted metapelitic enclaves and host dacite, SE Spain. *Journal of Petrology*, *51*(4), 785–821. doi.org/10.1093/petrology/egp095

Álvarez-Valero, A. M., Cesare, B., & Kriegsman, L. M. (2005). Formation of elliptical garnet in a metapelitic enclave by melt-assisted dissolution and reprecipitation. *Journal of Metamorphic Geology*, *23*(2), 65–74. doi.org/10.1111/j.1525-1314.2005.00562.x

Álvarez-Valero, A. M., & Kriegsman, L. M. (2007). Crustal thinning and mafic underplating beneath the Neogene Volcanic Province (Betic Cordillera, SE Spain): Evidence from crustal xenoliths. *Terra Nova*, *19*(4), 266–271. doi.org/10.1111/j.1365-3121.2007.00745.x

Álvarez-Valero, A. M., & Waters, D. J. (2010). Partially melted crustal xenoliths as a window into sub-volcanic processes: Evidence from the Neogene Magmatic Province of the Betic Cordillera, SE Spain. *Journal of Petrology*, *51*(5), 973–991. doi.org/10.1093/petrology/egq007

Andersen, T. (2002). Correction of common lead in U-Pb analyses that do not report 204 Pb. *Chemical Geology*, *192*, 59–79.

Anenburg, M., & Williams, M. J. (2022). Quantifying the tetrad effect, shape components, and Ce–Eu–Gd anomalies in rare earth element patterns. *Mathematical Geosciences*, *54*(1), 47-70.

Aranovich, L. Ya., & Podlesskii, K. K. (1983). The Cordierite-Garnet-Sillimanite-Quartz equilibrium: Experiments and applications. In S. K. Saxena (Ed.), *Advances in Physical Geochemistry* (Vol. 3, pp. 173–198). Springer, New York. doi.org/10.1007/978-1-4612-5587-1

Bach, P., Smith, I. E. M., & Malpas, J. G. (2012). The origin of garnets in andesitic rocks from the Northland arc, New Zealand, and their implication for sub-arc processes. *Journal of Petrology*, *53*(6), 1169–1195. doi.org/10.1093/petrology/egs012

Bartoli, O., Cesare, B., Poli, S., Acosta-Vigil, A., Esposito, R., Turina, A., Bodnar, R. J., Angel, R. J., & Hunter, J. (2013a). Nanogranite inclusions in migmatitic garnet: Behavior during piston-cylinder remelting experiments. *Geofluids*, *13*(4), 405–420. doi.org/10.1111/gfl.12038

Bartoli, O., Cesare, B., Poli, S., Bodnar, R. J., Acosta-Vigil, A., Frezzotti, M. L., & Meli, S. (2013b). Recovering the composition of melt and the fluid regime at the onset of crustal anatexis and S-type granite formation. *Geology*, *41*(2), 115–118. doi.org/10.1130/G33455.1

Bartoli, O., Tajčmanová, L., Cesare, B., & Acosta-Vigil, A. (2013c). Phase equilibria constraints on melting of stromatic migmatites from Ronda (S. Spain): Insights on the formation of peritectic garnet. *Journal of Metamorphic Geology*, *31*(7), 775–789. doi.org/10.1111/jmg.12044

Bédard, J. H., Dewing, K., Grasby, S. E., Nabelek, P., Hatlen Heimdal, T., Yakymchuk, C., Shieh, S. R., Rumney, J., Deegan, F. M., & Troll, V. R. (2023). Basaltic sills emplaced in organic-rich sedimentary rocks: Consequences for organic matter maturation and Cretaceous paleo-climate. *The Geological Society of America*. doi.org/doi.org/10.1130/B36982.1

Behar, F., Beaumont, V., & De, H. L. (2001). Technologie Rock-Eval 6: Performances et développements. *Oil and Gas Science and Technology*, *56*(2), 111–134. doi.org/10.2516/ogst:2001013

Berman, R. G. (1990). Mixing properties of Ca-Mg-Fe-Mn garnets. *American Mineralogist*, *75*, 328–344.

Berndt, C., Mjelde, R., Planke, S., Shimamura, H., & Faleide, J. I. (2001). Controls on the tectono-magmatic evolution of a volcanic transform margin: the Vøring Transform Margin, NE Atlantic. *Marine Geophysical Researches*, *22*, 133-152.

Berndt, C., Planke, S., Alvarez Zarikian, C. A., Frieling, J., Jones, M. T., Millett, J. M., Brinkhuis, H., Bünz, S., Svensen, H. H., Longman, J., Scherer, R. P., Karstens, J., Manton, B., Nelissen, M., Reed, B., Faleide, J. I., Huismans, R. S., Agarwal, A., Andrews, G. D. M., …

Yager, S. L. (2023). Shallow-water hydrothermal venting linked to the Palaeocene–Eocene Thermal Maximum. *Nature Geoscience*, *16*(9), 803–809. doi.org/10.1038/s41561-023-01246-8

Best, M. G., & Christiansen, E. H. (1997). Origin of broken phenocrysts in ash-flow tuffs. Geological Society of America Bulletin, 109(1), 63-73.

Biester, H., & Scholz, C. (1997). Determination of Mercury Binding Forms in Contaminated Soils: Mercury Pyrolysis versus Sequential Extractions. *Environmental Science & Technology*, *31*, 233–239.

Bindeman, I. N. (2005). Fragmentation phenomena in populations of magmatic crystals. American Mineralogist, 90(11-12), 1801-1815.

Bohlen, S. R., & Liotta, J. J. (1986). A barometer for garnet amphibolites and garnet granulites. *Journal of Petrology*, *27*, 1025–1034.

Branney, M. J., Brown, R. J., & Calder, E. (2021). Pyroclastic Rocks. In: Encyclopedia of Geology (Second Edition), edited by Alderton, S and Elias, S.A. Academic Press, Elsevier, https://doi.org/10.1016/B978-0-08-102908-4.00103-X

Celal Sengör, A. M., & Burke, K. (1978). Relative timing of rifting and volcanism on Earth and its tectonic implications. *Geophysical Research Letters*, *5*(6), 419–421.

Cesare, B., Acosta-Vigil, A., Ferrero, S., & Bartoli, O. (2011). Melt inclusions in migmatites and granulites. *Journal of the Virtual Explorer*, *38*. https://doi.org/10.3809/jvirtex.2011.00268

Cesare, B., & Gómez-Pugnaire, M. T. (2001). Crustal melting in the Alboran domain: Constraints from xenoliths of the Neogene volcanic province. *Physics and Chemistry of the Earth*, *26*, 255–260.

Cesare, B., Gómez-Pugnaire, M. T., & Rubatto, D. (2003). Residence time of S-type anatectic magmas beneath the Neogene Volcanic Province of SE Spain: A zircon and monazite SHRIMP study. *Contributions to Mineralogy and Petrology*, *146*(1), 28–43. doi.org/10.1007/s00410-003-0490-x

Cesare, B., Meli, S., Nodari, L., & Russo, U. (2005). Fe3+ reduction during biotite melting in graphitic metapelites: Another origin of CO2 in granulites. *Contributions to Mineralogy and Petrology*, *149*(2), 129–140. doi.org/10.1007/s00410-004-0646-3

Cesare, B., Ferrero, S., Salvioli-Mariani, E., Pedron, D., & Cavallo, A. (2009). "Nanogranite" and glassy inclusions: The anatectic melt in migmatites and granulites. *Geology*, *37*(7), 627–630. doi.org/10.1130/G25759A.1

1217 Cesare, G., Salvioli, E., & Venturelli, G. (1997). Crustal anatexis and melt extraction during
1218 deformation in the restitic xenoliths at E1 Joyazo (SE Spain). *Mineralogical Magazine*, *61*, 15–
1219 27.
1220 Chen, S., Wang, X., Niu, Y., Sun, P., Duan, M., Xiao, Y., Guo, P., Gong, H., Wang, G., & Xue,
1221 Q. (2017). Simple and cost-effective methods for precise analysis of trace element abundances in
1222 geological materials with ICP-MS. *Science Bulletin*, *62*(4), 277–289.
1223 doi.org/10.1016/j.scib.2017.01.004
1224 Chew, D. M., Petrus, J. A., & Kamber, B. S. (2014). U-Pb LA-ICPMS dating using accessory
1225 mineral standards with variable common Pb. *Chemical Geology*, *363*, 185–199.
1226 doi.org/10.1016/j.chemgeo.2013.11.006
1227 Clarke, D. B. (2007). Assimilation of xenocrysts in granitic magmas: principles, processes,
1228 proxies, and problems. *Canadian Mineralogist*, *45*, 5–30.
1229 Clemens, J. D., & Vielzeuf, D. (1987). Constraints on melting and magma production in the
1230 crust. *Earth and Planetary Science Letters*, *86*, 287–306.
1231 Clemens, J. D., & Wall, V. J. (1981). Origin and crystallization of some peraluminous (S-type)
1232 granitic magmas. *Canadian Mineralogist*, *19*, 111–131.
1233 Clemens, J. D., & Wall, V. J. (1988). Controls on the mineralogy of S-type volcanic and plutonic
1234 rocks. *Lithos*, *21*, 53–66.
1235 Clift, P. D., Carter, A., & Hurford, A. J. (1998). The erosional and uplift history of NE Atlantic
1236 passive margins: constraints on a passing plume. *Journal of the Geological Society*, *155*, 787–
1237 800.
1238 Comas, M. C., Platt, J. P., Soto, J. I., & Watts, A. B. (1999). The origin and tectonic history of
1239 the Alboran Basin: Insights from Leg 161 results. *Proceedings of the Ocean Drilling Program:*
1240 *Scientific Results*, *161*, 555–580. doi.org/10.2973/odp.proc.sr.161.262.1999
1241 Courtillot, V., Jaupart, C., Manighetti, I., Tapponnier, P., & Besse, J. (1999). On causal links
1242 between flood basalts and continental breakup. *Earth and Planetary Science Letters*, *166*, 177–
1243 195.
1244 Duggen, S., Hoernle, K., van den Bogaard, P., & Harris, C. (2004). Magmatic evolution of the
1245 Alboran region: The role of subduction in forming the western Mediterranean and causing the
1246 Messinian Salinity Crisis. *Earth and Planetary Science Letters*, *218*(1–2), 91–108.
1247 doi.org/10.1016/S0012-821X(03)00632-0

1248 Eggins, S. M., Kinsley, L. P. J., & Shelley, J. M. G. (1998). Deposition and element fractionation
1249 processes during atmospheric pressure laser sampling for analysis by ICP-MS. *Applied Surface*
1250 *Science*, *127*, 278–286.
1251 Elhlou, S., Belousova, E., Griffin, W. L., Pearson, N. J., & O'Reilly, S. Y. (2006). Trace element
1252 and isotopic composition of GJ-red zircon standard by laser ablation. *Goldschmidt Conference*
1253 *Abstracts*, *1*. doi:10.1016/j.gca.2006.06.1383
1254 Eide, C. H., Schofield, N., Howell, J., & Jerram, D. A. (2022). Transport of mafic magma
1255 through the crust and sedimentary basins: Jameson Land, East Greenland. *Journal of the*
1256 *Geological Society*, *179*(3). doi.org/10.1144/jgs2021-043
1257 Eldholm, O., Thiede, J., & Taylor, E. (1987). *7. Summary and preliminary conclusions, ODP leg*
1258 *104*. 751–771.
1259 Eldholm, O., Thiede, J., & Taylor, E. (1989). 51. Evolution of the Vøring volcanic margin.
1260 *Proceedings of the Ocean Drilling Program*, *104*, 1033–1065.
1261 Emeleus, C. H., Allwright, E. A., Kerr, A. C., & Williamson, I. T. (1996). Red tuffs in the
1262 Palaeocene lava successions of the Inner Hebrides. *Scottish Journal of Geology*, *32*(1), 83–89.
1263 Famelli, N., Millett, J. M., Hole, M. J., Lima, E. F., Carmo, I. D. O., Jerram, D. A., Jolley, D. W.,
1264 Pugsley, J. H., & Howell, J. A. (2021). Characterizing the nature and importance of lava-
1265 sediment interactions with the aid of field outcrop analogues. Journal of South American Earth
1266 Sciences, 108, 103108.
1267 Ferrand, T. P. (2020). Transition from amagmatic to volcanic margin: Mantle exhumation in the
1268 Vøring Basin before the Icelandic plume influence. *Tectonophysics*, *776*.
1269 doi.org/10.1016/j.tecto.2020.228319
1270 Ferrero, S., Bartoli, O., Cesare, B., Salvioli-Mariani, E., Acosta-Vigil, A., Cavallo, A., Groppo,
1271 C., & Battiston, S. (2012). Microstructures of melt inclusions in anatectic metasedimentary
1272 rocks. *Journal of Metamorphic Geology*, *30*(3), 303–322. doi.org/10.1111/j.1525-
1273 1314.2011.00968.x
1274 Frieling, J., Mather, T. A., März, C., Jenkyns, H. C., Hennekam, R., Reichart, G. J., Slomp, C. P.,
1275 & van Helmond, N. A. G. M. (2023). Effects of redox variability and early diagenesis on marine
1276 sedimentary Hg records. *Geochimica et Cosmochimica Acta*, *351*, 78–95.
1277 doi.org/10.1016/j.gca.2023.04.015

1278 Frieling, J., Svensen, H. H., Planke, S., Cramwinckel, M. J., Selnes, H., & Sluijs, A. (2016).
1279 Thermogenic methane release as a cause for the long duration of the PETM. *Proceedings of the*
1280 *National Academy of Sciences of the United States of America*, *113*(43), 12059–12064.
1281 doi.org/10.1073/pnas.1603348113
1282 Fitton, J.G., Saunders, A.D., Larsen, L.M., Fram, M.S., Demant, A., Sinton, C., and Leg 152
1283 Shipboard Scientific Party, 1995, Magma sources and plumbing systems during break-up of the
1284 SE Greenland margin: preliminary results from ODP Leg 152, *Journal of the Geological Society*
1285 *of London, 152*, p. 985-990.
1286 Fleitout, L., Froidevaux, C., Yuen, D., Fleitout, L., & Yuen, C. (1986). Active lithospheric
1287 thinning. *Tectonophysics*, *132*, 271.
1288 Fonneland, H. C., Lien, T., Martinsen, O. J., Pedersen, R. B., & Košler, J. (2004). Detrital zircon
1289 ages: A key to understanding the deposition of deep marine sandstones in the Norwegian Sea.
1290 *Sedimentary Geology*, *164*(1–2), 147–159. doi.org/10.1016/j.sedgeo.2003.09.005
1291 Gac, S., Abdelmalak, M. M., Faleide, J. I., Schmid, D. W., & Zastrozhnov, D. (2022). Basin
1292 modelling of a complex rift system: The Northern Vøring Volcanic Margin case example. *Basin*
1293 *Research*, *34*(2), 702–726. doi.org/10.1111/bre.12637
1294 Ghiorso, M. S., & Gualda, G. A. R. (2013). A method for estimating the activity of titania in
1295 magmatic liquids from the compositions of coexisting rhombohedral and cubic iron-titanium
1296 oxides. *Contributions to Mineralogy and Petrology*, *165*(1), 73–81. doi.org/10.1007/s00410-012-
1297 0792-y
1298 Gillard, M., Tugend, J., Müntener, O., Manatschal, G., Karner, G. D., Autin, J., Sauter, D.,
1299 Figueredo, P. H., & Ulrich, M. (2019). The role of serpentinization and magmatism in the
1300 formation of decoupling interfaces at magma-poor rifted margins. In *Earth-Science Reviews*
1301 (Vol. 196). Elsevier B.V. doi.org/10.1016/j.earscirev.2019.102882
1302 Giordano, D., Russell, J. K., & Dingwell, D. B. (2008). Viscosity of magmatic liquids: a model.
1303 Earth and Planetary Science Letters, 271(1-4), 123-134.
1304 Grasby, S. E., Them, T. R., Chen, Z., Yin, R., & Ardakani, O. H. (2019). Mercury as a proxy for
1305 volcanic emissions in the geologic record. In *Earth-Science Reviews* (Vol. 196). Elsevier B.V.
1306 doi.org/10.1016/j.earscirev.2019.102880
1307 Green, T. H. (1977). Garnet in silicic liquids and its possible use as a P-T indicator.
1308 *Contributions to Mineralogy and Petrology*, *65*, 59–67.

Green, T. H., & Ringwood, A. E. (1968). Origin of garnet phenocrysts in calc-alkaline rocks. *Contributions to Mineralogy and Petrology*, *18*, 163–174.

Gualda, G. A. R., Ghiorso, M. S., Lemons, R. v., & Carley, T. L. (2012). Rhyolite-MELTS: A modified calibration of MELTS optimized for silica-rich, fluid-bearing magmatic systems. *Journal of Petrology*, *53*(5), 875–890. doi.org/10.1093/petrology/egr080

Gutjahr, C. C. M. (1966). Carbonization of pollen grains and spores and their application: Leidse Geol. Meded., 38, 1-30.

Gutjahr, M., Ridgwell, A., Sexton, P. F., Anagnostou, E., Pearson, P. N., Pälike, H., Norris, R. D., Thomas, E., & Foster, G. L. (2017). Very large release of mostly volcanic carbon during the Palaeocene-Eocene Thermal Maximum. *Nature*, *548*(7669), 573–577. https://doi.org/10.1038/nature23646Harangi, SZ., Downes, H., Kosa, L., Szabo, CS., Thirlwall, M. F., Mason, P. R. D., & Mattey, D. (2001). Almandine garnet in calc-alkaline volcanic rocks of the Northern Pannonian Basin (Eastern-Central Europe): Geochemistry, petrogenesis and geodynamic implications. *Journal of Petrology*, *42*(10), 1813–1843.

Harley, S. L., & Carrington, D. P. (2001). The distribution of H2O between cordierite and granitic melt: H2O incorporation in cordierite and its application to high-grade metamorphism and crustal anatexis cordierites in several pegmatites and zones of hydrous fluid infiltration. *Journal of Petrology*, *42*.

Haynes, L. L., & Hönisch, B. (2020). The seawater carbon inventory at the Paleocene-Eocene Thermal Maximum. *PNAS Latest Articles*, 1–8. doi.org/10.1073/pnas.2003197117/-/DCSupplemental

Hill, R. I. (1991). Starting plumes and continental break-up. *Earth and Planetary Science Letters*, *104*, 398–416.

Holdaway, M. J. (2001). Recalibration of the GASP geobarometer in light of recent garnet and plagioclase activity models and versions of the garnet-biotite geothermometer. *American Mineralogist*, *86*, 1117–1129.

Holdaway, M. J., & Lee, S. M. (1977). Fe-Mg Cordierite Stability in High-Grade Pelitic Rocks Based on Experimental, Theoretical, and Natural Observations. *Contributions to Mineralogy and Petrology*, *63*, 175–198.

Holland, T. J. B., Green, E. C. R., & Powell, R. (2018). Melting of peridotites through to granites: A simple thermodynamic model in the system KNCFMASHTOCr. *Journal of Petrology*, *59*(5), 881–900. doi.org/10.1093/petrology/egy048

Holtz, F., Johannes, W., & Pichavant, M. (1992). Peraluminous granites: The effect of alumina on melt composition and coexisting minerals. *Transactions of the Royal Society of Edinburgh: Earth Sciences*, *83*(1–2), 409–416. doi.org/10.1017/S0263593300008075

Horni, J., Hopper, J. R., Blischke, A., Geisler, W. H., Stewart, M., Mcdermott, K., Judge, M., Erlendsson, Ö., & Árrting, U. (2017). Regional distribution of volcanism within the North Atlantic Igneous Province. *Geological Society Special Publication*, *447*(1), 105–125. doi.org/10.1144/SP447.18

Hoskin, P. W. O. (2005). Trace-element composition of hydrothermal zircon and the alteration of Hadean zircon from the Jack Hills, Australia. *Geochimica et Cosmochimica Acta*, *69*(3), 637–648. doi.org/10.1016/j.gca.2004.07.006

Huang, R., & Audétat, A. (2012). The titanium-in-quartz (TitaniQ) thermobarometer: A critical examination and re-calibration. *Geochimica et Cosmochimica Acta*, *84*, 75–89. doi.org/10.1016/j.gca.2012.01.009

Humphreys, M. C. S., Blundy, J. D., & Sparks, R. S. J. (2008). Shallow-level decompression crystallisation and deep magma supply at Shiveluch Volcano. *Contributions to Mineralogy and Petrology*, *155*(1), 45–61. doi.org/10.1007/s00410-007-0223-7

Jochum, K. P., Nohl, U., Herwig, K., Lammel, E., Stoll, B., & Hofmann, A. W. (2005). GeoReM: A new geochemical database for reference materials and isotopic standards. *Geostandards and Geoanalytical Research*, *29*, 333–338.

Jochum, K. P., Weis, U., Stoll, B., Kuzmin, D., Yang, Q., Raczek, I., Jacob, D. E., Stracke, A., Birbaum, K., Frick, D. A., Günther, D., & Enzweiler, J. (2011). Determination of reference values for NIST SRM 610-617 glasses following ISO guidelines. *Geostandards and Geoanalytical Research*, *35*(4), 397–429. doi.org/10.1111/j.1751-908X.2011.00120.x

Jones, M. T., Stokke, E. W., Rooney, A. D., Frieling, J., Pogge Von Strandmann, P. A. E., Wilson, D. J., Svensen, H. H., Planke, S., Adatte, T., Thibault, N., Vickers, M. L., Mather, T. A., Tegner, C., Zuchuat, V., & Schultz, B. P. (2023). Tracing North Atlantic volcanism and seaway connectivity across the Paleocene-Eocene Thermal Maximum (PETM). *Climate of the Past*, 19 (8), 1623-1652. https://doi.org/10.5194/cp-19-1623-2023

1369 Jones, S. M., Hoggett, M., Greene, S. E., & Dunkley Jones, T. (2019). Large Igneous Province
1370 thermogenic greenhouse gas flux could have initiated Paleocene-Eocene Thermal Maximum
1371 climate change. *Nature Communications*, *10*(1). doi.org/10.1038/s41467-019-12957-1
1372 Kanaris-Sotiriou, R. (1997). Graphite-bearing peraluminous dacites from the Erlend volcanic
1373 complex, Faeroe-Shetland Basin, North Atlantic. Mineralogical Magazine, 61(405), 175-184.
1374 Kanaris-Sotiriou, R., Morton, A.C., & Taylor, P.N. (1993). Palaeogene peraluminous
1375 magmatism, crustal melting and continental break-up: the Erlend complex, Faeroe-Shetland
1376 Basin, NE Atlantic. *Journal of the Geological Society London*, 150, 903–914.
1377 Kaneko, Y., & Miyano, T. (2004). Recalibration of mutually consistent garnet-biotite and garnet-
1378 cordierite geothermometers. *Lithos*, *73*(3–4), 255–269.
1379 https://doi.org/10.1016/j.lithos.2003.12.009
1380 Kelemen, P. B., & Holbrook, W. S. (1995). Origin of thick, high-velocity igneous crust along the
1381 US east coast margin. *Journal of Geophysical Research*, *100*(B6), 10077–10094.
1382 doi.org/10.1029/95jb00924
1383 Kender, S., Bogus, K., Pedersen, G. K., Dybkjær, K., Mather, T. A., Mariani, E., Ridgwell, A.,
1384 Riding, J. B., Wagner, T., Hesselbo, S. P., & Leng, M. J. (2021). Paleocene/Eocene carbon
1385 feedbacks triggered by volcanic activity. *Nature Communications*, *12*(1).
1386 doi.org/10.1038/s41467-021-25536-0
1387 Kennedy, A.K., Wotzlaw, J.F., Schaltegger, U., Crowley, J.L., Schmitz, M. (2014). Eocene
1388 zircon reference material for microanalysis of U-Th-Pb isotopes and trace elements. *The*
1389 *Canadian Mineralogist*, 52, 409-421. doi.org/10.3749/canmin.52.3.409
1390 Kennett, J., Stott, L. (1991). Abrupt deep-sea warming, palaeoceanographic changes and benthic
1391 extinctions at the end of the Palaeocene. *Nature* **353**, 225–229. https://doi.org/10.1038/353225a0
1392 Kirtland-Turner, S., & Ridgwell, A. (2016). Development of a novel empirical framework for
1393 interpreting geological carbon isotope excursions, with implications for the rate of carbon
1394 injection across the PETM. *Earth and Planetary Science Letters*, *435*, 1–13.
1395 doi.org/10.1016/j.epsl.2015.11.027
1396 Knox, B., & Morton, A. C. (1988). The record of early Tertiary N Atlantic volcanism in
1397 sediments of the North Sea Basin. *Geological Society Special Publication*, *39*, 407–419.
1398 Kylander-Clark, A. R. C., Hacker, B. R., & Cottle, J. M. (2013). Laser-ablation split-stream ICP
1399 petrochronology. *Chemical Geology*, *345*, 99–112. doi.org/10.1016/j.chemgeo.2013.02.019

1400 Lambart, S., Hamilton, S., Lang, O. I. (2022). Compositional variability of San Carlos olivine.
1401 *Chemical Geology*, *605*, 120968. https://doi.org/10.1016/j.chemgeo.2022.120968
1402 Larsen, H. C., & Saunders, A. D. (1994). 1. Introduction: Breakup of the southeast Greenland
1403 margin and the formation of the Irminger Basin: Background and scientific objectives.
1404 *Proceedings of the Ocean Drilling Program, Initial Reports*, *152*, 5–16.
1405 Le Breton, N., & Thompson, A. B. (1988). Fluid-absent (dehydration) melting of biotite in
1406 metapelites in the early stages of crustal anatexis. *Contributions to Mineralogy and Petrology*,
1407 *99*, 226–237.
1408 Li, X., Zhang, C., Almeev, R. R., & Holtz, F. (2020). GeoBalance: An Excel VBA program for
1409 mass balance calculation in geosciences. *Chemie Der Erde*, *80*(2).
1410 doi.org/10.1016/j.chemer.2020.125629
1411 Lu, G., & Huismans, R. S. (2021). Melt volume at Atlantic volcanic rifted margins controlled by
1412 depth-dependent extension and mantle temperature. *Nature Communications*, *12*(1).
1413 doi.org/10.1038/s41467-021-23981-5
1414 Ludwig, K. R. (1997). Optimization of multicollector isotope-ratio strontium and neodymium.
1415 *Chemical Geology*, *135*, 325–334.
1416 Luo, B., Zhang, H., Xu, W., Yang, H., Zhao, J., Guo, L., Zhang, L., Tao, L., Pan, F., & Gao, Z.
1417 (2018). The magmatic plumbing system for Mesozoic High-Mg andesites, garnet-bearing dacites
1418 and porphyries, rhyolites and leucogranites from West Qinling, Central China. *Journal of*
1419 *Petrology*, *59*(3), 447–482. doi.org/10.1093/petrology/egy035
1420 Luque, F. J., Barrenechea, J. F., & Rodas, M. (1993). Graphite geothermometry in low and high
1421 temperature regimes: two case studies. Geological Magazine, 130(4), 501-511.
1422 McDonough, W. F., & Sun, S. (1995). The composition of the Earth. *Chemical Geology*, *120*,
1423 223–253.
1424 McKenzie, N. R., Smye, A. J., Hegde, V. S., & Stockli, D. F. (2018). Continental growth
1425 histories revealed by detrital zircon trace elements: A case study from India. *Geology*, *46*(3),
1426 275–278. doi.org/10.1130/G39973.1
1427 Meyer, R., Hertogen, J., Pedersen, R. B., Viereck-Götte, L., & Abratis, M. (2009a). Interaction
1428 of mantle derived melts with crust during the emplacement of the Vøring Plateau, N.E. Atlantic.
1429 *Marine Geology*, *261*(1–4), 3–16. https://doi.org/10.1016/j.margeo.2009.02.007

1430 Meyer, R., Nicoll, G. R., Hertogen, J., Troll, V. R., Ellam, R. M., & Emeleus, C. H. (2009b).
1431 Trace element and isotope constraints on crustal anatexis by upwelling mantle melts in the North
1432 Atlantic Igneous Province: An example from the Isle of Rum, NW Scotland. *Geological*
1433 *Magazine*, *146*(3), 382–399. doi.org/10.1017/S0016756809006244
1434 Mjelde, R., Raum, T., Myhren, B., Shimamura, H., Murai, Y., Takanami, T., Karpuz, R., &
1435 Næss, U. (2005). Continent-ocean transition on the Vøring Plateau, NE Atlantic, derived from
1436 densely sampled ocean bottom seismometer data. *Journal of Geophysical Research: Solid Earth*,
1437 *110*(5), 1–19. doi.org/10.1029/2004JB003026
1438 Morton, A. C., Dixon, J. E., Fitton, J. G., Macintyre, R. M., Smythe, D. K., & Taylor, P. N.
1439 (1988a). Early Tertiary volcanic rocks in Well 163/6-1A, Rockall Trough. *Geological Society*
1440 *Special Publication*, *39*, 293–308.
1441 Neumann, E. R., Svensen, H., Tegner, C., Planke, S., Thirlwall, M., & Jarvis, K. E. (2013). Sill
1442 and lava geochemistry of the mid-Norway and NE Greenland conjugate margins. *Geochemistry,*
1443 *Geophysics, Geosystems, 14*(9), 3666–3690. https://doi.org/10.1002/ggge.20224
1444 Nielsen, C. H., & Sigurdsson, H. (1981). Quantitative methods for electron microprobe analysis
1445 of sodium in natural and synthetic glasses. *American Mineralogist, 66*, 547–552.
1446 Owen, G. (1987). Deformation processes in unconsolidated sands. Geological Society, London,
1447 Special Publications, 29(1), 11-24.
1448 Pearson, D. G., Emeleus, C. H. & Kelley, S. P. (1996) Precise $^{40}Ar/^{39}Ar$ age for the initiation of
1449 Palaeogene volcanism in the Inner Hebrides and its regional significance. *Journal of the*
1450 *Geological Society of London, 153,* 815-818
1451 Pedersen, T., Heeremans, M., & van der Beek, P. (1998). Models of crustal anatexis in volcanic
1452 rifts: Applications to southern Finland and the Oslo Graben, southeast Norway. *Geophysical*
1453 *Journal International*, *132*(2), 239–255. doi.org/10.1046/j.1365-246x.1998.00416.x
1454 Perchuck, L. L., Aranovich, L. Ya., Podlesskii, K. K., Lavrant'Eva, I. v., Gerasimov, V. Yu.,
1455 Fed'Kin, V. V., Kitsul, V. I., Karsakov, L. P., & Berdnikov, N. v. (1985). Precambrian granulites
1456 of the Aldan shield, eastern Siberia, USSR. *Journal of Metamorphic Geology*, *3*(3), 265–310.
1457 doi.org/10.1111/j.1525-1314.1985.tb00321.x
1458 Pereira, M., & Bea, F. (1994). Cordierite-producing reactions in the Pena Negra Complex, Avila
1459 Batholith, Central Spain: The key role of cordierite in low-pressure anatexis. *The Canadian*

Mineralogist, *32*, 763–780. http://pubs.geoscienceworld.org/canmin/article-pdf/32/4/763/3446537/763.pdf

Peron-Pinvidic, G., Manatschal, G., & Osmundsen, P. T. (2013). Structural comparison of archetypal Atlantic rifted margins: A review of observations and concepts. In *Marine and Petroleum Geology* (Vol. 43, pp. 21–47). https://doi.org/10.1016/j.marpetgeo.2013.02.002

Planke, S., Berndt, C., Alvarez Zarikian, C.A., Agarwal, A., Andrews, G.D.M., Betlem, P., Bhattacharya, J., Brinkhuis, H., Chatterjee, S., Christopoulou, M., Clementi, V.J., Ferré, E.C., Filina, I.Y., Frieling, J., Guo, P., Harper, D.T., Jones, M.T., Lambart, S., Longman, J., Millett, J.M., Mohn, G., Nakaoka, R., Scherer, R.P., Tegner, C., Varela, N., Wang, M., Xu, W., and Yager, S.L. (2023a). Expedition 396 summary. In Planke, S., Berndt, C., Alvarez Zarikian, C.A., and the Expedition 396 Scientists, Mid-Norwegian Margin Magmatism and Paleoclimate Implications. Proceedings of the International Ocean Discovery Program, 396: College Station, TX (International Ocean Discovery Program). doi: 10.14379/iodp.proc.396.101.2023.

Planke, S., Berndt, C., Alvarez Zarikian, C.A., Agarwal, A., Andrews, G.D.M., Betlem, P., Bhattacharya, J., Brinkhuis, H., Chatterjee, S., Christopoulou, M., Clementi, V.J., Ferré, E.C., Filina, I.Y., Frieling, J., Guo, P., Harper, D.T., Jones, M.T., Lambart, S., Longman, J., Millett, J.M., Mohn, G., Nakaoka, R., Scherer, R.P., Tegner, C., Varela, N., Wang, M., Xu, W., and Yager, S.L. (2023b). Sites U1569 and U1570. In Planke, S., Berndt, C., Alvarez Zarikian, C.A., and the Expedition 396 Scientists, Mid-Norwegian Margin Magmatism and Paleoclimate Implications. Proceedings of the International Ocean Discovery Program, 396: College Station, TX (International Ocean Discovery Program). doi: 10.14379/iodp.proc.396.106.2023

Planke, S., Rasmussen, T., Rey, S. S., & Myklebust, A. (2005). Seismic characteristics and distribution of volcanic intrusions and hydrothermal vent complexes in the Vøring and Møre basins. *Petroleum Geology: North-West Europe and Global Perspectives— Proceedings of the 6th Petroleum Geology Conference*, 833844.

Platt, J. P., Soto, J. I., Whitehouse, M. J., Hurford, A. J., & Kelley, S. P. (1998). Thermal evolution, rate of exhumation, and tectonic significance of metamorphic rocks from the floor of the Alborán extensional basin, western Mediterranean. *Tectonics*, *17*(5), 671–689. https://doi.org/10.1029/98TC02204

Polteau, S., Planke, S., Zastrozhnov, D., Abdelmalak, M. M., Lebedeva-Ivanova, N., Planke, E. E., Svensen, H. H., Mazzini, A., Gernigon, L., Myklebust, R., Kjølhamar, B. E., Pedersen, R. B.,

1491 Sandstå, N. R., & Bünz, S. (2020). Upper Cretaceous-Paleogene stratigraphy and development of
1492 the Mìmir High, Vøring Transform Margin, Norwegian Sea. *Marine and Petroleum Geology*,
1493 *122*. https://doi.org/10.1016/j.marpetgeo.2020.104717
1494 Pouchou, J.-L., & Pichoir, F. (1991). Quantitative analysis of homogeneous of stratified
1495 microvolumes applying the model "PAP." *Electron Probe Quantitation*, 31–75.
1496 Pownceby, M. I., Wall, V. J., & StC, H. O. (1987). Mn partitioning between garnet and ilmenite:
1497 experimental calibration and applications. *Contributions to Mineralogy and Petrology*, *97*, 116–
1498 126.
1499 Pownceby, M. I., Wall, V. J., & O'Neill, H. St. C. (1991). An experimental study of the effect of
1500 Ca upon garnet-ilmenite Fe-Mn exchange equilibria. *American Mineralogist*, *76*, 1580–1588.
1501 Rampino, M. R. (2013). Peraluminous igneous rocks as an indicator of thermogenic methane
1502 release from the North Atlantic Volcanic Province at the time of the Paleocene-Eocene Thermal
1503 Maximum (PETM). *Bulletin of Volcanology*, *75*(1), 1–5. doi.org/10.1007/s00445-012-0678-x
1504 Riel, N., Kaus, B. J. P., Green, E. C. R., & Berlie, N. (2022). MAGEMin, an Efficient Gibbs
1505 Energy Minimizer: Application to Igneous Systems. *Geochemistry, Geophysics, Geosystems*,
1506 *23*(7). doi.org/10.1029/2022GC010427
1507 Roche, O., Niño, Y., Mangeney, A., Brand, B., Pollock, N., & Valentine, G. A. (2013). Dynamic
1508 pore-pressure variations induce substrate erosion by pyroclastic flows. Geology, 41(10), 1107–
1509 1110.
1510 Rudnick, R. L., & Gao, S. (2003). Composition of the Continental Crust. *Treatise on*
1511 *Geochemistry*, *3*, 1–64.
1512 Saunders, A. D., Jones, S. M., Morgan, L. A., Pierce, K. L., Widdowson, M., & Xu, Y. G.
1513 (2007). Regional uplift associated with continental large igneous provinces: The roles of mantle
1514 plumes and the lithosphere. *Chemical Geology*, *241*(3–4), 282–318.
1515 doi.org/10.1016/j.chemgeo.2007.01.017
1516 Senda, R., Kimura, J. I., & Chang, Q. (2014). Evaluation of a rapid, effective sample digestion
1517 method for trace element analysis of granitoid samples containing acid-resistant minerals: Alkali
1518 fusion after acid digestion. *Geochemical Journal*, *48*(1), 99–103.
1519 doi.org/10.2343/geochemj.2.0280
1520 Sieck, P., López-Doncel, R., Dávila-Harris, P., Aguillón-Robles, A., Wemmer, K., & Maury, R.
1521 C. (2019). Almandine garnet-bearing rhyolites associated to bimodal volcanism in the Mesa

Central of Mexico: Geochemical, petrological and geochronological evolution. *Journal of South American Earth Sciences*, *92*, 310–328. doi.org/10.1016/j.jsames.2019.03.018

Siivola, J. (1969). On the evaporation of some alkali metals during the electron microprobe analyses. In *Bulletin of the Geological Society of Finland*, *41*, 85-91.

Sinton, C. W., Hitchen, K., & Duncan, R. A. (1998). 40Ar–39Ar geochronology of silicic and basic volcanic rocks on the margins of the North Atlantic. *Cambridge University Press*, *135*(2), 161–170.

Sláma, J., Košler, J., Condon, D. J., Crowley, J. L., Gerdes, A., Hanchar, J. M., Horstwood, M. S. A., Morris, G. A., Nasdala, L., Norberg, N., Schaltegger, U., Schoene, B., Tubrett, M. N., & Whitehouse, M. J. (2008). Plešovice zircon - A new natural reference material for U-Pb and Hf isotopic microanalysis. *Chemical Geology*, *249*(1–2), 1–35. doi.org/10.1016/j.chemgeo.2007.11.005

Sparks, R. S. J., Sigurdsson, H., & Carey, S. N. (1980a). The entrance of pyroclastic flows into the sea, II. Theoretical considerations on subaqueous emplacement and welding. Journal of Volcanology and Geothermal Research, 7(1-2), 97-105.

Sparks, R. S. J., Sigurdsson, H., & Carey, S. N. (1980b). The entrance of pyroclastic flows into the sea I. Oceanographic and geologic evidence from Dominica, Lesser Antilles. Journal of Volcanology and Geothermal Research, 7(1-2), 87-96.

Spear, F. S., & Selverstone, J. (1983). Water exsolution from quartz: Implications for the generation of retrograde metamorphic fluids. *Geology*, *11*, 82–85.

Spear, F.S., 1993. Metamorphic Phase Equilibria and Pressure–Temperature–Time Paths. *Mineralogical Society of America*, Washington, D. C. (799 pp.).

Staplin, F. L. (1969). Sedimentary organic matter, organic metamorphism, and oil and gas occurrence. Bulletin of Canadian Petroleum Geology, 17(1), 47-66.

Stearns, M. A., Bartley, J. M., Bowman, J. R., Forster, C. W., Beno, C. J., Riddle, D. D., Callis, S. J., & Udy, N. D. (2020). Simultaneous magmatic and hydrothermal regimes in alta-little cottonwood stocks, Utah, USA, recorded using multiphase U-Pb petrochronology. *Geosciences (Switzerland)*, *10*(4). doi.org/10.3390/geosciences10040129

Stevens, G., Villaros, A., & Moyen, J. F. (2007). Selective peritectic garnet entertainment as the origin of geochemical diversity in S-type granites. *Geology*, *35*(1), 9–12. doi.org/10.1130/G22959A.1

Stevens, G., Clemens, J. D., & Droop, G. T. R. (1995). Hydrous cordierite in granulites and crustal magma production. *Geology*, *23*, 925–928.

Storey, M., Duncan, R. A., & Swisher III, C. C. (2007). Paleocene-Eocene Thermal Maximum and the opening of the Northeast Atlantic. *Science*, *316*(5824), 587–589. doi.org/10.1126/science.1138751

Sun, S., McDonough W.F. (1989). Chemical and isotopic systematics of oceanic basalts: implications for mantle composition and processes *Geological Society, London, Special Publications*, 42, 1, pp. 313-345

Svensen, H. H., Jones, M. T., Percival, L. M. E., Grasby, S. E., & Mather, T. A. (2023). Release of mercury during contact metamorphism of shale: Implications for understanding the impacts of large igneous province volcanism. *Earth and Planetary Science Letters*, *619*. doi.org/10.1016/j.epsl.2023.118306

Svenson, H., Planke, S., Maithe-Sørensen, A., Jamtveit, B., Myklebust, R., Eidem, T. R., & Rey, S. S. (2004). Release of methane from a volcanic basin as a mechanism for initial Eocene global warming. *Nature*, *429*(6991), 542–545. doi.org/10.1038/nature02566

Sykes, M. L., & Holloway, J. R. (1987). Magmatic processes: Physicochemical principles evolution of granitic magmas during ascent: A phase equilibrium model. *The Geochemical Society*, 447–461.

Takahashi, T., Shuto, K. (1997). Major and trace element analyses of silicate rocks using X-ray fluorescence spectrometer RIX3000. *Rigaku-Denki J*. 28, 25–37.

Taylor, J., & Stevens, G. (2010). Selective entrainment of peritectic garnet into S-type granitic magmas: Evidence from Archaean mid-crustal anatectites. *Lithos*, *120*(3–4), 277–292. doi.org/10.1016/j.lithos.2010.08.015

Tera, F., & Wasserburg, G. J. (1972). U-Th-Pb systematics in three Apollo 14 basalts and the problem of initial Pb in lunar rocks. *Earth and Planetary Science Letters*, *14*, 281–304.

Thomas, J. B., Watson, E. B., Spear, F. S., Shemella, P. T., Nayak, S. K., & Lanzirotti, A. (2010). TitaniQ under pressure: The effect of pressure and temperature on the solubility of Ti in quartz. *Contributions to Mineralogy and Petrology*, *160*(5), 743–759. doi.org/10.1007/s00410-010-0505-3

Thompson, A. B. (1976). Mineral reactions in pelitic rocks: II. calculations of some P-T-X (Fe-Mg) phase relations. *American Journal of Science*, *276*, 425–454.

Thorarinsson, S., Holm, P., Tappe, S., Heaman, L., Tegner, C. (2011). Late Cretaceous–Paleocene continental rifting in the High Arctic: U-Pb geochronology of the Kap Washington Group volcanic sequence, North Greenland. J. Geol. Soc. 168, 1093–1106

Thybo, H., & Artemieva, I. M. (2013). Moho and magmatic underplating in continental lithosphere. In *Tectonophysics*, *609*, 605–619. doi.org/10.1016/j.tecto.2013.05.032

Tugend, J., Gillard, M., Manatschal, G., Nirrengarten, M., Harkin, C., Epin, M. E., Sauter, D., Autin, J., Kusznir, N., & McDermott, K. (2018). Reappraisal of the magma-rich versus magma-poor rifted margin archetypes. *Geological Society Special Publication*, *476*(1), 23–47. doi.org/10.1144/SP476.9

Turner, S. P., Platt, J. P., George, R. M. M., Kelley, S. P., Pearson, D. G., & Nowell, G. M. (1999). Magmatism Associated with Orogenic Collapse of the Betic-Alboran Domain, SE Spain. *Journal of Petrology*, *40*, 1011–1036.

Vermeesch, P. (2018) IsoplotR: a free and open toolbox for geochronology. *Geoscience Frontiers, 9*, p.1479-1493, doi: 10.1016/j.gsf.2018.04.001.

Vickers, M.L., Jones, M.T., Longman, J., Evans, D., Ullmann, C.V., Stokke, E.W., Vickers, M., Frieling, J., Harper, D.T., Clementi, V.J., & the IODP Expedition 396 Scientists (2023). Paleocene-Eocene age glendonites from the Norwegian Margin – Indicators of cold snaps in the hothouse? *EGUsphere [preprint]*, https://doi.org/10.5194/egusphere-2023-1651.

Viereck, L. G., Taylor, P. N., Parson, L. M., Morton, A. C., Hertogen, J., & Gibson, I. L. (1988). Origin of the Palaeogene Vøring Plateau volcanic sequence. *Geological Society Special Publication*, *39*, 69–83. doi.org/10.1144/GSL.SP.1988.039.01.08

Vissers, R. L. M., Platt, J. P., & van der Wal, D. (1995). Late orogenic extension of the Betic the Alboran Domain: A lithospheric view. *Tectonics*, *14*(4), 786–803.

Vry, J., Brown, P. E., & Valley, J. W. (1990). Cordierite volatile content and the role of CO2 in high-grade metamorphism. *American Mineralogist*, *75*, 71–88. https://www.researchgate.net/publication/282494760

Wark, D. A., & Watson, E. B. (2006). TitaniQ: A titanium-in-quartz geothermometer. *Contributions to Mineralogy and Petrology*, *152*(6), 743–754. https://doi.org/10.1007/s00410-006-0132-1

Wells, P. R. A. (1979). Chemical and thermal evolution of Archaean Sialic crust, Southern West Greenland. *Journal of Petrology*, *20*, 187–226. http://petrology.oxfordjournals.org/

Westerhold, T., Marwan, N., Drury, A. J., Liebrand, D., Agnini, C., Anagnostou, E., Barnet, J. S. K., Bohaty, S. M., de Vleeschouwer, D., Florindo, F., Frederichs, T., Hodell, D. A., Holbourn, A. E., Kroon, D., Lauretano, V., Littler, K., Lourens, L. J., Lyle, M., Pälike, H., … Zachos, J. C. (2020). An astronomically dated record of Earth's climate and its predictability over the last 66 million years. *Science*, *369*, 1383–1387.

White, A. J. R., & Chappell, B. W. (1977). Ultrametamorhpism and granitoid genesis. *Tectonophysics*, *43*, 7–22.

White, J. D. (2000). Subaqueous eruption-fed density currents and their deposits. Precambrian Research, 101(2-4), 87-109.

White, R. S., Spence, G. D., Fowler, S. R., McKenzie, D. P., Westbrook, G. K., & Bowen, A. N. (1987). Magmatism at rifted continental margins. *Nature*, *330*(3), 439–444.

White, R., & McKenzie, D. (1989). Magmatism at rift zones: the generation of volcanic continental margins and flood basalts. *Journal of Geophysical Research*, *94*(B6), 7685–7729. doi.org/10.1029/JB094iB06p07685

White, R. S., Smith, L. K., Roberts, A. W., Christie, P. A. F., Kusznir, N. J., Roberts, A. M., Healy, D., Spitzer, R., Chappell, A., Eccles, J. D., Fletcher, R., Hurst, N., Lunnon, Z., Parkin, C. J., & Tymms, V. J. (2008). Lower-crustal intrusion on the North Atlantic continental margin. *Nature*, *452*(7186), 460–464. doi.org/10.1038/nature06687

Wiedenbeck, M., Hanchar, J. M., Peck, W. H., Sylvester, P., Valley, J., Whitehouse, M., Kronz, A., Morishita, Y., Nasdala, L., Fiebig, J., Franchi, I., Girard, J. P., Greenwood, R. C., Hinton, R., Kita, N., Mason, P. R. D., Norman, M., Ogasawara, M., Piccoli, P. M., … Zheng, Y. F. (2004). Further characterisation of the 91500 zircon crystal. *Geostandards and Geoanalytical Research*, *28*(1), 9–39. doi.org/10.1111/j.1751-908X.2004.tb01041.x

Wilkinson, C. M., Ganerød, M., Hendriks, B. W. H., & Eide, E. A. (2017). Compilation and appraisal of geochronological data from the North Atlantic Igneous Province (NAIP). *Geological Society*, *447*, 69–103. doi.org/10.6084/m9.figshare.c.3554472

Wu, C. M., & Zhao, G. C. (2006). The applicability of the GRIPS geobarometry in metapelitic assemblages. *Journal of Metamorphic Geology*, *24*(4), 297–307. doi.org/10.1111/j.1525-1314.2006.00638.x

Wu, C. M. (2019). Original calibration of a garnet geobarometer in metapelite. *Minerals*, *9*(9). doi.org/10.3390/min9090540

1646 Zeck, H. P. (1970). An erupted migmatite from Cerro del Hoyazo, SE Spain. Contributions to
1647 Mineralogy and Petrology, 26, 225-246.
1648 Zeck, H. P. (1992). Restite-melt and mafic-felsic magma mixing and mingling in an S-type
1649 dacite, Cerro del Hoyazo, southeastern Spain. Earth and Environmental Science Transactions of
1650 the Royal Society of Edinburgh, 83(1-2), 139-144.
1651 Zeebe, R. E., Ridgwell, A., & Zachos, J. C. (2016). Anthropogenic carbon release rate
1652 unprecedented during the past 66 million years. *Nature Geoscience*, *9*(4), 325–329.
1653 doi.org/10.1038/ngeo2681
1654 Zeebe, R. E., Zachos, J. C., & Dickens, G. R. (2009). Carbon dioxide forcing alone insufficient
1655 to explain Palaeocene-Eocene Thermal Maximum warming. *Nature Geoscience*, *2*(8), 576–580.
1656 doi.org/10.1038/ngeo578